



POLITECNICO DI TORINO  
Repository ISTITUZIONALE

Microstructural characterization of solid oxide fuel cell electrodes by image analysis technique

*Original*

Microstructural characterization of solid oxide fuel cell electrodes by image analysis technique / LANZINI A.; LEONE P.; ASINARI P. - In: JOURNAL OF POWER SOURCES. - ISSN 0378-7753. - 194 Issue 1(2009), pp. 408-422.

*Availability:*

This version is available at: 11583/2364364 since:

*Publisher:*

Elsevier

*Published*

DOI:10.1016/j.jpowsour.2009.04.062

*Terms of use:*

openAccess

This article is made available under terms and conditions as specified in the corresponding bibliographic description in the repository

*Publisher copyright*

(Article begins on next page)

# Microstructural characterization of SOFC electrodes by image analysis technique

## Abstract

This paper deals with the microstructural characterization of electrodes of solid oxide fuel cells based on processing of 2D images. The interest relies on the reliable description of the structures that determine the microscopic image by means of parameters involving the morphology, the shape and the size of elementary structures, and the microscopic topology in terms of spatial connectivity functions among the structures. The use of detailed mathematical methods allowed one to reconstruct the 3D structure of both fuel and air electrodes having 2D images as input.

The analysis was applied to an anode supported cell with NiO based anode, 8YSZ electrolyte and LSM/YSZ cathode. The microscopic analysis was performed by means of both a SEM and an optical microscope before and after the electrical testing of the cell.

The obtained images were processed and a quantitative analysis was performed achieving information concerning the microstructure and including: phases' fraction, grain size, granulometry law, constituent shape factors, phase spatial organization and descriptive functions. The microstructure features were analyzed by means of one-point and two-point statistics. It was possible to build 3D structures of the electrodes: anode and the double-layer cathode.

The work also stresses out some aspects related to the reliable use of the observed microscopic parameters and topology functions as inputs for electrodes' modelling. In the work, the results of the image analysis are used with a simple analytical model with the aim to estimate the optimal design of the cathode current functional layer (CFL). It was showed that the actual cell design with 15  $\mu\text{m}$  thick CFL was optimized for a temperature as high as 850  $^{\circ}\text{C}$  with a charge transfer and total ohmic resistance of around 0.2  $\Omega\text{cm}^2$ . More generally, results of image analysis can be used efficiently as input in the multi-scale modelling of SOFC electrodes considering macroscopic and mesoscopic models.

**Keywords:** image analysis, SOFC modeling, electrode design, nickel coarsening.

## **1. Introduction**

### **1.1 General considerations**

Solid oxide fuel cells are considered a promising technology matching the energy vision of tomorrow, that is high efficiency, pollution free operation, multi-fuel capability. Several issues are under investigations and concern the use of low-cost and effective manufacturing procedures, the increase of cell power density with the reduction of the operating temperature, the understanding and limitation of degradation phenomena related to its long-term operation. In this scenario, the reliable microscopic analysis of the cells is of very importance and it has high relevance. The capability of analyze microscopic features is a key discriminator for design of high performance and robust fuel cells. The evaluation of location of reaction sites in the electrodes, the charge transport properties of manufactured layers, the micro-fluidic properties of reactive species and the evolution of micro-structure due to degradation phenomena are only possible coupling high quality microstructural analysis and modelling.

This papers deals with an experimental analysis of SOFC ceramic flat plates in order to analyze and evaluate the design, with some further considerations regarding the degradation processes. A reliable description of the microstructures of the electrodes was conducted by means of parameters involving the morphology, the shape and the size of elementary structures, and the microscopic topology in terms of spatial connectivity functions among the structures.

### **1.2 Overview of image analysis techniques**

Advanced techniques for cell characterization are recently indicated as prior to enhance the quality of research in fuel cells and push the technology into levels for market penetration. Advanced methods include the possibility to characterize microscopic features, mechanical properties and thermal properties of cells, often in relation to steady state or transient operating conditions [1-5].

In particular images analysis techniques and structures reconstruction methods have been proposed as powerful and reliable tools in the fuel cell research. Studies by Scanning Electron Microscopy SEM are limited to scales of micron and submicron. Transmission Electron Microscope (TEM) is the preferred analytical technique on a nanoscale level but traditionally, the use of TEM for interface study in SOFC was rather limited due to the difficulties in specimen preparation [6]. Recently, Focused Ion Beam (FIB) technique has become an effective method for TEM specimen preparation. FIB TEM enables 3-D analysis of electrode microstructure: particle and pore size and distribution, triple-phase boundary density, pore tortuosity [3, 4]. However image analysis techniques applied to SOFCs have been investigated since few year ago also using classical approaches. These methods remain nowadays the most popular for the easiness to perform them without high cost equipments, but rather with instrumentation having already a large-diffusion. Image analysis techniques have been proposed by Simwonis et al. [7] to evaluate degradation of Ni/YSZ anodes in SOFCs. Ni-granulometry curves of operated cells after different operational times were reported. Lee et Al. investigate the anode's microstructure of a Ni cermet anode generating elemental maps of the main solid species and pores [8] and afterwards they use some information to estimate the electrical properties of electrodes using electrochemical methods [9, 10]. In [11] 3D structural reconstructions of fuel cells electrodes are achieved using methods based on one-point statistics or the granulometry law and two-point statistics which provides a more reliable reconstruction since it takes into account porosity and the two-point auto-correlation function which provides information about the connectivity of the pores in the porous medium. The reconstructed topologies of PEM and SOFC electrodes are then analyzed in terms of their micro-fluidic properties. Image analysis is also used to evaluate degradation phenomena and evolution the microstructures during steady state [7] and transients operation [5]. 3D structure reconstructions have been also achieved using an experimentally-based approach with FIB technique coupled with TEM analysis [3].

Information obtained from image analysis can be then used in modelling, including cell performance and degradation phenomena. Many research focused on micro-modelling of fuel cells [12-21], results led to encouraging indications and conclusions about cell optimization. An optimized microstructure of a cermet electrode should have long-range connectivity of respective ionic and electronic conductor chains stretching across the electrode and linking the current collector to the electrolyte; and maximized active sites of three-phase boundary (TPB) for electrochemical reactions. These requirements warrant an optimal ratio of ionic to electronic conductors, in terms of their volume and average grain size, in a properly sintered electrode. In addition to the required microstructure for enhancing conversion of ionic to electronic current taking place at the TPB and transport of these currents along their respective “active bond” (chains), there is other important consideration such as efficient gas diffusion from the bulk into the reaction sites.

The charge transport properties were well identified and discussed in [16,17,18,19, 21] and some experimental results on commercial cells confirmed the results achieved in that analysis [19]. While gas diffusion in a solid phase of a SOFC electrodes were detailed faced by Asinari et al. in [22].

### **1.3 Overview of the work of this paper**

In this paper, digital images related to electrodes’ microstructures were obtained from different techniques (SEM, Energy Dispersive Spectrometer – EDS, optical microscope), they were then processed and a quantitative analysis was performed achieving information concerning the microstructure and including: phases’ fraction, grain size, granulometry law, constituent shape factors, phase spatial organization and descriptive functions. The micro-structure features were analyzed by means of one-point and two-point statistics. It was possible to build 3D structures of the main cell’s layers using truncated gaussian methods [23].

An image analysis procedure has been developed to determine the main morphological and geometrical properties of the investigated cell. Once collected SEM and optical images, they have

been analyzed through an in-house developed code and a new software called CHIMERA® [24]. Contrast enhancing and noise filtering plus others common image adjusting settings has been used to eliminate defects in the acquired images. Regarding the porous electrodes, the adjusted images has been then bounded to distinguish the porous phase form the solid phase (binary thresholding). With some images has been also possible to distinguish of the solid fraction of the electrode, the electronic phase (Ni for the anode, and LSM for the cathode) and ionic phase (8YSZ for both electrodes). This allowed us to perform a micro-modeling of the composite electrodes to estimate their electrical and electrochemical performances.

The analysis was applied to brand new cells and tested cells pointing out degradation phenomena such as the nickel agglomeration; in particular, we made a detailed analysis of the microscopic features of SOFC layers including anodes and double-layers cathodes pointing out to the cathode design and the anode microstructure degradation.

The information obtained by the image analysis was also used combined with analytical models in order to estimate the design properties of the layers. We focused our work on some models presented in the previously discussed works, in particular on the charge transfer model and the percolation theory, since they showed good agreement with experimental data. We modelled every cell's layer, with particular attention to the cathode functional layer, since it is expected to be a major source of losses in the cell. Our main objective has been to determine if such commonly used models, that describe the electrical and electrochemical properties of SOFC composite electrodes (such as LSM/8YSZ for cathode, and Ni/8YSZ for anode) are good to predict the optimum design configuration, which essentially means the proper designing of electrodes porosity, grain size of particles, volume fraction of the ionic and the electronic phases, thickness of active layers and current-collecting layers, etc.. The work also stresses out some aspects related to the reliable use of the observed microscopic parameters as inputs for those models. To perform this effectively, we considered a commercial SOFC planar cell produced by INDEC® (ASC1 cell), which deploys composite electrodes and whose design is later described. We took into account the work presented

in another published paper [25], where some electrical and electrochemical macroscopic parameters were extrapolated through parameter estimation from experimental polarization curves. Of the estimated parameters, we used the estimation of the  $i_{0,cat}$  (equilibrium exchange current density) as an input to define the charge transfer resistance,  $R_{ct,eff}$ , of the ASC1 active cathode layer (which is used in model of effective charge transfer by Tanner et al. [12, 13]). Then we coupled microscopic observations of the cell's electrodes, obtained through image analysis techniques, and the calculated  $R_{ct,eff}$  was employed to evaluate the actual design of the ASC1 active cathode in terms of geometrical and microstructural parameters. In particular, the cell design is evaluated simulating different cathode functional layer and it is concluded that the present design of the cell is optimized for operating at a temperature as high as 850°C. A thicker electrode is required for minimize losses at lower temperature. Moreover, the obtained results can be used as input in multi-scale modelling approaches from analytical to complex mesoscopic models [22].

## 2. Experimental

### 2.1 Experimental Setup: polarization analysis

The tests were performed with circular shaped anode supported SOFC cells from InDEC®, with a diameter of 80 mm and an active area of 47 cm<sup>2</sup>. The actual macroscopic geometrical features were determined from SEM of the cells. The geometry and materials of the cell were:

- (ASC1): anode 525-610 μm thick with two layers (both made of NiO/8YSZ cermet: functional layer 5-10 μm thick; support layer 520-600 μm thick); electrolyte 4-6 μm thick Y<sub>0.16</sub>Zr<sub>0.84</sub>O<sub>2</sub> (8YSZ), with unknown volume density; cathode 30-40 μm thick with two layers (functional layer of porous 8YSZ and La<sub>0.75</sub>Sr<sub>0.2</sub>MnO<sub>3</sub> (LSM); current collecting layer of LSM alone).

The cell run around 200 hours with 0.5 l/min of hydrogen humidified at 30°C and 1.5 l/min of air at the cathode side. The cell were tested in the range between 650°C and 850°C taking several polarization curves and in generally operating at relative low current load (0.3 A/cm<sup>2</sup>) and fuel utilization factors higher than 40%. Further details about the test-rig have been presented in [25].

## 2.2 Experimental Setup: microscopy analysis

The information about the microstructural properties of the ASC1 cell was obtained from both a scanning electron microscope (SEM) ZEISS EVO 40 and an optical microscope LEICA REICHERT MeFe3.

We focused our analysis on the same type of cell (ASC1), viewed firstly as brand new and subsequently after that complete polarisation test session was performed. The reason for this was not only to evaluate degradation phenomena occurring on an anode-supported cell, but also to evaluate the microstructural characteristics of the cell under operating conditions after the NiO is reduced to metallic Ni. The reduction step occurs when hydrogen is flowed to cell and could be considered in same way as the last step of the manufacturing of a cell. The microstructural change of a cell after anode reduction is quite significant. In [26] Hannappel et al. have studied the effect of the reduction temperature on the subsequent cell electrochemical behaviour, seeing that at higher temperature of reduction the cell performances improve. In a previous work [27], we demonstrated that after the reduction step, the Young modulus of an anode supported planar SOFC decreased from 108 to 50 GPa.

Our cell has been reduced at a temperature of 800 °C. During the heating-up phase the anode side is fed by a 500 ml/min flow of N<sub>2</sub>; after the set-point temperature is reached, the nitrogen flow is gradually substituted by hydrogen.

## 3. Methodology of microscopic analysis

After collecting a set of images for the whole cell and each of its functional layers, we evaluated the average thickness of each layer. Subsequently, for the composite electrodes (anode support and active cathode) we evaluated their porosity, the volume fraction and distribution of the solid and pore phases along with their mean grain sizes. These morphological properties have been estimated by the software CHIMERA®; details on how this software works and how we used it for our



purposes are described in the next paragraph. This software has been developed essentially to be helpful for oil companies in the recovery efforts of oil and gas from underground and undersea reservoirs. It allows one to analyze images of porous and/or composite media, to distinct each phase present in it, and eventually reconstruct a 3D model structure from 2D image samples in order to evaluate important properties such as permeability of the fluid phase, capillarity pressure in the fluid channels, etc. We found out that the tools of CHIMERA® could be useful as well for the field of fuel cells and their microstructural and morphological characterization.

In **Table 1**, the main steps of the image analysis procedure we adopted are summarized.

### **Table 1 – Steps for analyzing the collected images**

#### **3.1 Microscopic properties of ASC1 electrodes**

As said before, we performed our image analysis through the software CHIMERA®. The strong features of this software, compared to other available commercial software such as FOVEA PRO® (a plug-in tool-box of ADOBE PHOTOSHOP® to perform image-analysis) are i) several binarization methods to extrapolate each phase from a composite structure to make more accurate the binarization step and compare uncertainties related with each method; ii) deeper mathematical methods used to analyse the distribution of each phase and to reconstruct the 3D structure having 2D binary images as input, iii) easy tool to average granulometry distribution curves and manage even large set of images. In Paragraph 3.2 we illustrate in a synthetic way the methodology we followed to analyze SEM and optical images of new and operated ASC1 cells in order to gather important information on the very fine structure of composite electrodes and their materials composition and distribution.

### 3.2 Image analysis for a Ni/8YSZ anode support

This paragraph reports the procedure presented above, and deployed in this paper to analyze the anode support structure of an ASC1 cell. The same procedure has been used for all the images characterized in this paper.

First we collected several back-scattered SEM images of grinded and polished sections of a brand new ASC1 cell. The back-scattering electrons detector allows one to have different intensity of color intensity in a gray-scale depending on the atomic number of the material from which the electron is scattered. For a composite structure such as that of a Ni/8YSZ anode, this microscopic imaging technique is really helpful to distinguish each phase from another. In particular the anode structure is porous as well and three different phases can be distinguished, two solids, the NiO or Ni phase (depending on whether the reduction step has already occurred or not) and the 8YSZ phase, and one void, due to the pores of the electrode. The resolution for this set of SEM images, with a magnitude of 1000x, is 3.6 pixels/ $\mu\text{m}$ ; this value is obtained directly from the micron bars shown on each image.

Then we took into consideration just five images of the anode support section in order to evaluate average properties of this component. This is not a statistically meaningful set, and the right way to handle this would be to develop a software tool which extracts hundreds of sub-pictures from the experimental ones and then it repeats the following procedure. This is what are we are planning to do in our future works on image analysis.

The selected images have then been adjusted and filtered from noise and other disturbs through the commercial software. This is similar to what done by Lee et al. in their work on image analysis [8,9]. The scope of this is to help to well distinguish each phase of the composite electrode before the binarization step.

For each image, once enhanced and corrected through the CHIMERA, we binarized and extrapolated the pores phase as shown below.

After this, we isolate each phase through the thresholding procedure. From the gray histogram of the selected image we decide where to truncate the gray curve determining which pixels belong to a certain phase and which not. The output is three binarized images; each of one representing just the pixels in a certain gray interval for that particular phase, that namely are the “Pores” phase, the “Ni” phase and the “Zr” phase. Actually with this last label we refer to the YSZ material.

This is somewhat an arbitrary method, which makes all the image analysis procedure somewhat arbitrary. However this is unavoidable, because, in order to separate each phase from another, it is necessary to define some threshold levels in the grayscale which allow one to define that all the pixels ranging in a certain grayscale interval belong to a univocal phase. Since each image always differs from the others (for example in terms of contrast, luminosity and other parameters), the thresholding process is neither simple nor an automatic step. However, high quality images usually reduce the sensitivity of the obtained post-processing results from the adopted thresholds.

In **Figure 1**, below, is showed one of the ASC1 composite anode SEM image taken under consideration for this work. As said before, the images have been taken in back-scattering in order to better discriminate not only the pores phase from the solid ones, but also to distinguish ion and electron conducting materials. As just stated, since the image has taken by back-scattered electrons, it possible to distinguish the solid phase due to Ni from that one due to Zr. Since the Ni has a higher atomic number, the Ni-phase is the gray one, besides the white one is attributed to the Zr-phase.

**Figure 1 – SEM Image of ASC1 anode support after the step of image adjusting and contrast enhancing**

In **Figure 2**, it is shown how the pores phase of the anode region represented in **Figure 1** has been separated from the others phase. This is binarization step can be easily performed either by many commercial software for image analysis. It is generally possible only to separate each phase at once; for this reason, we developed a homemade simple code that starting from an SEM-BSE image,

separates the original image pixels in the phases that constitutes it and shows maps of each phase, accounting for the number of pixels belonging to each phase. The threshold levels have been user-defined taking into account the image histogram shaping, as shown in **Figure 3**. The output of the binarized phases is then showed in **Figure 4**.

**Figure 2 - Binary image of the pores phase of image of Figure 1**

**Figure 3 – Grayscale histogram shaping of the anode image reported in **Figure 1****

**Figure 4 – Binarized images of each phase present in **Figure 1****

The same work has been conducted using the EDS element mapping with the OXFORD Instruments® microanalysis equipment installed on our SEM microscope. The region scanned with EDS is reported below, in **Figure 5**. The output mapped image is shown then in **Figure 6**. The aim was to perform the binarization of each phase using as source an image where Ni and YSZ phase were both distinguishable through a techniques other than back-scattering. Through EDS mapping with green color the Ni element is mapped, and with red color the Zr element. We actually succeed very well in this operation, as shown in the in Figure 8, where we selected a small region of the precedent image (Figure 7); it is clearly visible a very large agglomerate of Ni.

**Figure 6. Top) SEM BSE image of whole cell section**

**Figure 7. EDS mapping of Ni (green) and Zr (red)**

**Figure 8. a) SEM BSE image of selected region for EDS mapping; b) EDS element mapping of selected region (Red: Ni, Green: Zr).**

The purpose was to show that EDS mapping can be an alternative technique to acquire images of composite electrodes in order to have ionic phase well-distinguishable from the electronic phase. Also optical images confirmed the validity of our preceding statement by EDS analysis. However, EDS mapping takes longer to be performed and is not straight-forward to set appropriately the

microscope parameters in order to acquire good and reliable maps. For these reasons, in this work, we used essentially BSE images for image analysis.

At the top of the SEM image in Figure 6, are visible the cathodic double layer, and the thin 8YSZ electrolyte; the rest of the image is the anode support. The biggest black holes are large pores that could represent residual air bubble in the tape-casted anode slurry. Apart from them, the porosity appears homogeneously distributed and has been estimated by image thresholding as 26 %.

In what following we describe the procedure for the characterization of a single binarized phase, e.g. the pore phase. The analysis presented below has been repeated exactly the same manner for the two other phases present in anode (namely the YSZ phase, and the Ni phase).

We took into account five SEM-BSE pictures at 1000x, representing different region of anode support of ASC1. For each image, we calculated the distribution of the pores radius (Figure 9). In Figure 10 we report the mean distribution for those reported in Figure 9.

**Figure 9 – Comparison of pores distribution from 5 samples of ASC1 anode support**

**Figure 10 – Average pores distribution for an ASC1 anode support**

The same results concerning the Ni phase are reported in Figure 11 and 12.

**Figure 11 – Comparison of Ni distribution from 5 samples of ASC1 anode support**

**Figure 12 – Average Ni distribution for an ASC1 anode support**

It is worth the effort to point out that the Ni grain size distribution refers to Ni still being an oxide, since we considered a never-operated cell. We will show later how the Ni phase agglomerates in an operated cell spreading the actual distribution towards higher equivalent radii.

To complete our first discussion on the granulometry distribution of the phases of a composite electrode we present a summary of the average distribution of the “Ni”, “Zr” and “Pores” phases for the five images object of our demonstrative analysis (Figure 13).

**Figure 13 – Average phases distributions for an ASC1 anode support**

The mean grain size for each phase is estimated by the software upon the granulometry distribution presented above. These are relevant values since they are used for electrodes microscopic models presented in the next paragraphs.

In Table 2 are reported the values of porosity, volume fraction of each phase, mean grain size and thickness of the anode electrode analyzed in this paragraph through image analysis. In this same table are reported the results of cathode double layer, studied in Paragraph 3.3.

Once the binarized images for each phase of a composite electrode are available, in our case a SOFC anode support, we can perform zero and first order statistics operations in order to extract quantitative information in 2D binary images (phase fraction, grain size, particles and pore distribution) and to describe the topology of each phase. The term topology indicates the spatial connectivity relations between the image objects. This is possible since the acquired digital images are considered as a stochastic [and random](#) process. This allows one to simplify the analysis of image properties and characteristics. Then, in a binary image we can define the so-called phase functions which are associated to each phase constituting the image:

$$Z_{\Gamma}(\mathbf{x}) = \begin{cases} 1, & \text{if } \mathbf{x} \text{ belongs to phase } \Gamma \\ 0, & \text{if not} \end{cases}, \quad \text{Eq. 1}$$

where  $\mathbf{x} = (i, j)$  represents a position vector with regards to a reference origin, and  $\Gamma$  can be either one phase or another. It is presumed, a priori, that the microstructure representative images have statistical homogeneity.

Since we consider the images as stochastic processes, we can describe their properties by mathematically defined [statistical](#) quantities. In particular, we consider proper integrals of the phase functions designed to capture both global and detailed geometric information about the image. Clearly the application of the integral operator allows one to get rid of most of the unessential details, with the exception of those which are useful to characterize the image as a whole. For example, if we consider a given pixel (i.e. elementary discretization) in an image, by observing the chance of this pixel belonging to a pore, a one-point statistics is recovered. The same concept can

be obtained by integrating the corresponding phase function and normalizing the result. For this reason, from a statistical point of view, the volume fraction of a solid phase of a composite structure or its porosity (being the pores just another phase of the structure) is a proper integral of the corresponding phase function. Going deeper in our examination by observing the chance of two random pixels belonging to a pore, we can define a two-point autocorrelation function, and so on for defining multiple-point autocorrelation functions.

For a SOFC electrode we can describe each phase by the porosity as:

$$\phi_{\Gamma} = \langle Z_{\Gamma}(\mathbf{x}) \rangle, \quad \text{Eq. 2}$$

where the operator  $\langle \rangle$  represents the normalized spatial integral over the domain defined by the considered image.

For stochastic processes a correlation function is the correlation between random variables at two different points in space or time. If one considers the correlation function between random variables at the same point but at two different times then one refers to this as the autocorrelation function.

For image analysis purposes, the two-point autocorrelation function is then defined as (see Adler et al. in [23]):

$$R_z(u) = \frac{\langle [Z_{\Gamma}(\mathbf{x}) - \phi_{\Gamma}][Z_{\Gamma}(\mathbf{x} + \mathbf{u}) - \phi_{\Gamma}] \rangle}{\phi_{\Gamma} - \phi_{\Gamma}^2}, \quad \text{Eq. 3}$$

for each random dislocation in the image plane. Furthermore, with the hypothesis of an isotropic medium, the correlation depends only on  $u = |\mathbf{u}|$ , which represents a spatial dislocation in the image plane. Regarding its practical meaning, the autocorrelation function gives us the probability of two pixels separated by the distance  $u$  of belonging to the same phase  $\Gamma$ .

With the hypothesis of a statistically homogenous electrode, the autocorrelation function for each phase  $\Gamma$ , mathematically defined by Eq. 2, can be practically calculated on the binarized images replacing the denominator of the second term in Eq. 3 by the following term, called simply correlation function:

$$\begin{aligned} C_{\Gamma}(u) &= \langle Z_{\Gamma}(\mathbf{x}) Z_{\Gamma}(\mathbf{x} + \mathbf{u}) \rangle \\ C_{\Gamma}(u) &= \langle Z_{\Gamma}(i, j) Z(i + u, j) \rangle, \end{aligned} \quad \text{Eqs. 4}$$

being  $i$  and  $j$  the coordinates of a generic pixel on the image plane.

The latter expressions are derived considering that for each phase the binarized image  $S$  is divided into two sub-sets, namely say  $S_1$  and  $S_2$ , being  $S = S_1 \cup S_2$  and  $S_1 \cap S_2 = \emptyset$ ; in order to calculate  $C_{\Gamma}(u)$ ,  $S_1$  is translated by a distance  $u$  along the  $i$ -axis; it yields  $S_1(+u)$ . The spatial average indicated in Eq. 4 is then replaced by an intersection of images:

$$\langle Z(i, j) Z(i + u, j) \rangle = S_1(+u) \cap S. \quad \text{Eq. 5}$$

Then for calculating the expression in Eq. 2, the denominator term is evaluated just as presented, while the other operations are simply algebraically performed.

If the dislocation is not just along a single axis, but in multiple directions, we could write a more general form of Eqs. 4, which could be:

$$C_{\Gamma}(u, v) = \langle Z_{\Gamma}(i, j) Z_{\Gamma}(i + u, j + v) \rangle. \quad \text{Eq. 6}$$

The commercial code allows one to determine the autocorrelation function for the binarized images. The default method is the spatial method, which considers dislocation of the image in one direction only (Eq. 5). This method can present large fluctuations, even though this is not the case for the binary images analyzed in this paper. Anyway, in case of large fluctuations, it is possible to consider the frequential method, which is basically equivalent to consider all the possible dislocations in all directions. In practice, the result obtained is equivalent to determining the spatial autocorrelation function in all directions (at  $360^\circ$ ).



The correlation functions for each binarized phase of the anode, obtained by the spatial method (just one direction considered), are presented in Figures 14-16.

**Figure 14 – “Ni” phase spatial correlation function**

**Figure 15 – “Ni” phase spatial correlation function**

**Figure 16 – “Pores” phase spatial correlation function**

From the spatial correlation function is possible through the commercial software to reconstruct in 3D the phase structure. The method used is the Truncated-Gaussian method. This method is described by Adler et al. [23] and its fundamental hypothesis states that a porous microstructure can be fully described by the one-point and two-point statistics of its phase function. It also considers that the porous microstructures are statistically homogeneous and isotropic. The porous media is constructed in a discrete manner; it is composed of  $N_c^3$  small elementary cubes, each having size  $w$ , which corresponds to the pixel of the analyzed image. These elementary cubes correspond either to pore or solid phase. The structure is then generated filling a certain volume with these elementary cubes, each of one either belonging or not to the phase selected to be reconstructed, and being given the phase porosity and autocorrelation function. Basically the use of the Truncated-Gaussian method consists in the generation of a random space function  $Z(\mathbf{x})$ , which is equal to 0 in the solid phase, and 1 in the pore phase. As already stated, the random generation of the structure takes place having as constraints the average statistical quantities described before, i.e. the porosity  $\phi$  and the autocorrelation function  $R_Z(\mathbf{x})$ , and the fact that the generated 3D structure has a finite size  $w \cdot N_c$  (being this product the cube length  $L_c$ ).

The method for generating discrete random variables, which verify Eqs. 2 and 3, is provided by Adler et al. [23] and Quiblier et al. [28], and was further developed by Z.R. Liang et al. [39].

Adler (1990) and Quiblier (1984) showed that a random and discrete field can be devised from a non-correlated Gaussian field  $X(\mathbf{x})$  when the latter one is successively passed through a linear and nonlinear filter. This can be realized in two steps starting from Gaussian and independent field called here  $X(\mathbf{x})$ . The random variables  $X(i,j,k)$  of the starting Gaussian field are assumed to be

normally distributed with mean equal to 0 and a variance equal to 1; these variables are also independent. Linear combinations of these variables by means of the coefficient field  $a$  yield a population  $Y(\mathbf{x})$  which is still Gaussian but correlated; clearly the correlation depends upon the coefficient field of the linear combination. A linear operator can be defined by an set of coefficients  $a(\mathbf{u}')$ , where  $\mathbf{u}'$  is the discrete displacement belonging to the discrete cube  $[0, L_c]^3$ . Outside this cube, the  $a(\mathbf{u}')$  takes the zero value. A new random field  $Y(\mathbf{x})$  which passes through a linear filter can be expressed as linear combination of the random variable  $X(\mathbf{x})$  as following:

$$Y(\mathbf{x}) = \sum_{\mathbf{u}' \in [0, L_c]^3} a(\mathbf{u}') X(\mathbf{x}_t), \quad \text{Eq. 7}$$

being the translated vector  $\mathbf{x}_t = \mathbf{x} + \mathbf{u}'$ . Periodic boundary conditions apply in order to deal with the finite cube  $N_c^3$ . It can be shown that the random variables  $Y(\mathbf{x})$  are Gaussian and centered, under proper conditions [23]. The autocorrelation function  $R_Y(\mathbf{u})$  of  $Y(\mathbf{x})$  can be derived as [23]:

$$R_Y(\mathbf{u}) = \sum_{r, s, t \in [0, L_c]^3} a(r, s, t) a(r + \mathbf{u}, s, t), \quad \text{Eq. 8}$$

where  $\mathbf{u} + r$  and period boundary conditions apply again. The random variables  $Y(i, j, k)$  have a standard normal distribution, though they are not statistically independent anymore. So the  $Y(\mathbf{x})$  field is correlated, but it still not satisfactory since it takes its values in real number set, while the porous structure to be reconstructed has to be represented by a discrete-value function  $Z(\mathbf{x})$ .

Hence the population  $Y(\mathbf{x})$  is transformed into a discrete population  $Z(\mathbf{x})$  which takes only two values, 0 and 1, and the average value of is automatically set equal to the value of  $\phi_T$ ; this last transformation can be considered as a nonlinear filter. The random variables  $X(i, j, k)$  are assumed to be normally distributed with a mean equal to zero and a variance equal to one and they are uncorrelated. In order to extract  $Z(\mathbf{x})$  form  $Y(\mathbf{x})$ , one applies a nonlinear filter  $G$ , which is a deterministic function of  $Y(\mathbf{x})$  [23]:

$$Z = G(Y). \quad \text{Eq. 9}$$

Once  $G$  is known, the statistical properties of the random field  $Z(\mathbf{x})$  can be derived from the properties of  $Y(\mathbf{x})$ . Since the random variable  $Y(\mathbf{x})$  has a standard normal distribution, its distribution function  $P(y)$  is given by

$$P(y) = \frac{1}{\sqrt{2\pi}} \int_{-\infty}^y e^{-y^2/2} dy. \quad \text{Eq. 10}$$

The deterministic function  $G$  is defined in the following way. When the random variable  $Y$  is equal to  $y$ ,  $Z$  takes the value  $z$ :

$$\begin{cases} z = 1 & \text{when } P(y) \leq \phi_r \\ z = 0 & \text{otherwise} \end{cases}. \quad \text{Eq.11}$$

In this way the average value of  $Z(\mathbf{x})$  is equal to  $\phi_r$  and its variance to  $\phi_r - \phi_r^2$ .

This procedure by Adler and Quiblier is analogous to solving an inverse problem, since it is necessary to determine the coefficients  $a$  and the correlation function  $R_Y(u)$  before being able to reconstruct the porous structure. The mathematical determination of  $R_Y(u)$  is described in details in Adler [23], as well as for the determination of the  $a$  coefficients. The difficulty associated with the use of the linear filter presented above is to determine  $a(\mathbf{u}')$  by solving Eq. 8, which is a nonlinear system of equations. Generally solving this system of equations is time-consuming, difficult, and sometimes even not possible.

For these reasons Z.R. Liang et al. (1998) in [39] showed how is possible to avoid the linear filter using Fourier transforms. They overcome this problem by the help of a mathematical theorem which enabled them to find an alternative way to generate the Gaussian field. Basically they generated the field  $Y(\mathbf{x})$  from  $X(\mathbf{x})$  using Fourier transform. From a computational point of view, then use of the fast Fourier transform algorithm, instead of laborious solution of nonlinear equations, represents a more preferable approach rather than using the linear filter method. The difference between the two methods is that with the Fourier transform  $Y(\mathbf{x})$  is directly generated from its autocorrelation function  $R_Y(u)$  and does not need the filter passing through  $X(\mathbf{x}) \rightarrow Y(\mathbf{x})$ .

This latter approach using Fourier transforms is the one used by the software CHIMERA® in the 3D reconstruction tool using the reconstruction method defined as the Truncated-Gaussian Method. Next we present some representative 3D structure image output obtained with the commercial code using the Truncated-Gaussian method (Figures 17-18). The sources for reconstructing the 3D structures are the binarized 2D phase images along with the calculated spatial-correlation function.

**Figura 17- Ni phase 3D reconstruction (cube 27.8x27.8x27.8  $\mu\text{m}^3$ )**

**Figure 18 – Pores phase 3D reconstruction (cube 27.8x27.8x27.8  $\mu\text{m}^3$ )**

These 3D structure could be used in a Lattice Boltzmann Method (LBM) code to compute the diffusion of reactants gases to the anode electrode, evaluating specific fluidynamic quantities, such as tortuosity [11,22]. The reconstruction of the Ni phase could be used, instead, for computing the flow of the electronic charge. Actually, the commercial software allows one to reconstruct just a phase at once, according to the mathematic method described before. The limit lays in the Truncated-Gaussian method, which considers just a medium with two phases. For this reason, it is not currently possible using this method to have a simultaneous reconstruction of each phase of a SOFC composite electrode, which has three phases (two solid and one void, the pore phase). Actually we can reconstruct one phase at once considering the other two phase as the rest. So it is possible to obtain the 3D reconstruction of the whole structure. The problem is then putting together the tree reconstructions in the same volume space, preserving the correlation function of each phase created separately. This a limitation if one would evaluate for example the Three Phase Boundaries (TPB) of the electrode, which requires having a volume filled simultaneously with the all three phases.

### 3.2.1 Nickel agglomeration

The coarsening of Nichel in an anode composite structure is a phenomenon well described in [29-33]. As far as the Ni/YSZ cermet anodes are concerned, the most predominant microstructure

change is the agglomeration and coarsening of Ni phase. The phenomenon has been investigated from a microscopic point of view through image analysis techniques revealing an increase of the mean particle size of Ni particles. The main reason for the agglomeration of Ni in the Ni/YSZ system is probably due to the poor wettability between the metallic Ni and YSZ oxide phase. Nikolopoulos et al. [29,30] studied the wettability and interface reaction between Ni and YSZ system in the temperature range of 1250–1500°C and purified Ar/4%H<sub>2</sub> atmosphere. Molten Ni showed no wettability towards YSZ ceramic phase ( $\theta = 117^\circ$ ). Additives such as Ti, Cr, Mn and Pd have certain effect on the wettability between Ni and YSZ. However, the effect on the interfacial energy of the Ni/YSZ system appears to be small. Due to low melting temperature, pure Ni has a high tendency to sinter at SOFC operation temperatures (e.g., 1000 °C). The sintering of pure Ni anodes in reducing environment is very rapid, leading to the formation of isolated islands. Therefore, the prevention or reduction of agglomeration and sintering of metallic Ni phase in the Ni/YSZ cermet electrodes rely heavily on the microstructure optimization of the Ni/YSZ cermets. In Figure 19, is shown the cross-section of an ASC1 cell before and after testing.

**Figure 19 – Cross section of an ASC1 anode support before (left) and after (right) testing.**

Seeing the Ni structure agglomerated in some regions of a brand new cell, means that Ni has formed these agglomerates during the anode sintering (last step of the component manufacturing). However, as shown later in this paper, this phenomenon takes also considerably place during the cell operation life. In order to show that, we compared the Ni-phase distribution in a brand new cell with that in an operated cell (as shown in Figure 19) of the same type. What we suspected to be Ni agglomerates were confirmed by the EDS analysis. If we assume that the darker gray phase is Ni, it is important to note how the Ni-phase tends to form some large agglomerated, even if homogeneously distributed over the anode section. For checking this phenomenon, we evaluated the distribution of the Ni phase in a cell brand new and operated (Figure 20).

### **Figure 20. Comparison of Ni-phase granulometry in a ASC1 cell before and after testing**

It is really interesting to report the large Nickel agglomeration that was occurred in the cell after a short operational life (about 300 hours). Very large “islands” of Ni are present. In the next section we try to evaluate the impact of this degradation phenomenon on the cell electrical behaviour using the percolation theory.

In Figure 21, another close-up of the anode of an operated cell clearly shows the phenomena of nickel coarsening.

### **Figure 21 – Ni agglomeration in a used cell**

### **3.3 Microscopic properties of cathode**

The study of the microstructure of cathodic double layer is somewhat more difficult compared to that of the anode layer. This is due to its materials composition, to its much finer microstructure and the reduced thickness of the layers. In Figures 22-24 we present the cross-sections images of the double layer cathode we utilized for the image analysis. By the means of EDS microscopy, it was hard to distinguish the ionic phase (YSZ) from the electronic one (LSM). The two phases appear to have a similar grain structure and they are also highly mixed together. This is for improving the actives sites for H<sub>2</sub> reduction, but it also makes image analysis not easy to perform. Anyway with SEM BSE detector finally we succeeded in determine the fraction volumes of YSZ and LSM.

**Figure 22. SEM image of the ASC1 cell (from top to bottom: Ni/8YSZ anode support, 8YSZ dense electrolyte, LSM/8YSZ active layer, LSM porous current collector layer)**

**Figure 23. SEM image of the cathode current collector layer**

**Figure 24 - SEM-BSE micrograph of the whole cell cross-section**

In Figures 25-26 we report the binarized distribution of each phase for the active layer, and the current collector layer (as done previously on the anode electrode). We estimated the porosity of the

active layer and the current collector layer as well. Basically for the cathode electrode we repeated the same image analysis conducted on the anode.

**Figure 25. Solid and pore phase distribution and volume fraction estimated through image analysis of the cathode active layer**

**Figure 26. Solid and pore phase distribution and volume fractions estimated through image analysis of the cathode current collector layer**

Figures 25-26 show different porosity between the cathode active layer and current collector layer. This is because the current collector layer mainly acts as a diffusion layer, letting the oxidant penetrate the active layer, where the electrochemical reaction effectively takes place. The reason why the latter layer is denser, lays on the fact that the composite solid phase made of LSM/8YSZ realizes a charge-transfer phenomenon instead of a mass transport phenomena.

We do not report again the correlation functions calculated for each binarized phase since we already showed this type of result for the anode, we just report as an example output of 3D structure of LSM porous current collector layer (Figure 27).

**Figure 27 - (at left) 3D reconstruction of the porous cathode current collector layer (cube 20x20x20  $\mu\text{m}^3$ ); (at right) close-up of the reconstructed structure**

#### **4. Micro-models of composite electrodes**

Image analysis is very powerful when its results can be used for modelling purposes. The high quality of information presented in this paper can be used in a multi-scale modelling approach starting from analytical microscopic models up to 3D electrical modelling of the electrodes and micro-fluidic modelling of the reactive species flowing through the pores.

In this paragraph, the information obtained by the image analysis will be used in order to estimate the cell design (ASC1) and its nominal operating temperature according to the investigated microstructure and using analytical models based on charge transfer and percolation theories

**([12,13,15,16,18,20,21]).**

#### 4.1 Methodology of electrochemical analysis

The electrochemical characterization was performed by taking V-I measurements over a range of temperatures between 750 °C and 850 °C with hydrogen as fuel, and air as oxidant. Then polarization curves were analyzed using a polarization model and by statistical regression on the experimental data. Parameter estimation method was used in order to break-down the main contribution of polarization resistance of the cell. Parameters such as effective exchange current density, ohmic resistance and anodic limiting current densities were obtained. The aim is to obtain macroscopic parameters describing the electrochemical performance and thus link them with the microscopic properties of the cell. Further details can be found in our previous work [25].

The cell voltage is expressed by equation 12:

$$V_c = V_{Nernst} - \frac{R \cdot T}{\alpha_{eff} \cdot F} a \sinh\left(\frac{i}{2 \cdot I_{o,eff}}\right) - R_{\Omega} \cdot i + \frac{R \cdot T}{2 \cdot F} \log\left(1 - \frac{i}{i_{as}}\right) + \frac{R \cdot T}{4 \cdot F} \log\left(1 - \frac{i}{i_{cs}}\right) \quad \text{Eq. 12}$$

The Nernst potential,  $V_{Nernst}$ , was assumed equal to the measured open circuit voltage. The activation overvoltage was modeled using a single-term equation of the hyperbolic sine approximation of the Butler-Volmer equation. This is equal to assume one of the equilibrium exchange current densities sufficiently larger than the other, thus allowing the corresponding activation loss to be neglected [34]. The ohmic resistance in the model takes into account the resistance of electrolyte, electrodes, interface resistance and any contact resistance between current collectors. Concerning limitations in mass transport, it is expected that the anode is the critical electrode, so the anodic limiting current density is chosen to treat this losses and it is estimated through the fitting procedure; at the cathode a value of limiting current density is fixed.

The results of the fitting procedure are resumed in Figure 28. Further details can be found in [25].

#### 4.2 Relation between the cell's electrochemical performance and microstructure



In the latter paragraph, the electrochemical analysis of the ASC1 cell combining current-voltage experiments and estimation of macroscopic parameters of a lumped polarization model was achieved. In particular the charge transfer limitations were modelled with the estimation of an effective exchange current density. An effective charge transfer resistance can be subsequently defined [12]:

$$\eta_{act} \cong \frac{R \cdot T}{z \cdot F \cdot I_{O,C}} \cdot i = R_{ct}^{eff} \cdot i \quad \text{Eq. 13}$$

The effective exchange current densities were 197 mA/cm<sup>2</sup>, 112 mA/cm<sup>2</sup> and 60 mA/cm<sup>2</sup> at 840, 800 and 740 °C, respectively. The following values can be then obtained for the effective charge transfer resistance, 0.12 Ω cm<sup>2</sup> at 840 °C, 0.21 Ω cm<sup>2</sup> at 800 °C and 0.36 Ω cm<sup>2</sup> at 740 °C. In order to evaluate the actual design in terms of charge transfer polarization it was then possible to obtain the value of the intrinsic charge transfer resistance. This was done considering the equation developed by Tanner et Al. ([13]), the actual cell microscopic values and electrochemical macro-parameters [25]. The estimated values of intrinsic charge transfer resistance were 2 Ω cm<sup>2</sup> at 840 °C, 3.6 Ω cm<sup>2</sup> at 800 °C and 6.2 Ω cm<sup>2</sup> at 740 °C. A first result is that the effective charge transfer resistance is decreased of more than one order of magnitude with the use of the composite layer [12, 13].

In Figure 29 it is drawn the evaluation of charge transfer resistance for different cathode functional layer thickness, also the design point is indicated. Curves are traced for the three different temperature levels tested in the analysis. The actual microscopic topology of the electrode seems to be really effective for the reduction of charge transfer resistance and it approaches the asymptotic limit given by the theory.

In addition to the charge transfer resistance, it was also important to estimate the overvoltage related to the ohmic resistance. In general the ohmic resistance is a sum of several contributors [35]: electrolyte, cathode functional layer (CFL), cathode current collecting layer (CCCL), anode

functional layer (AFL), anode current collecting layer (ACCL) and resistances at interfaces and contact resistance. In terms of equation this is expressed by:

$$R_{\Omega} = R_{8YSZ} + R_{LSM/8YSZ} + R_{LSM} + R_{Ni/YSZ} + R_{Ni/YSZ} + R_{contact} \quad [\Omega \cdot cm^2] \quad \text{Eq. 14}$$

In particular the following values of ohmic cell resistances were estimated: 0.135 at 840 °C, 0.189 at 800 °C and 0.322 at 740 °C [25]. The dependence of the ohmic loss on temperature was estimated through apparent thermal activation energy of Arrhenius equation and its value was 0.89 eV, the interpolating equation was:

$$\log_{10}(\sigma \cdot T) = -5103/T + 5.13 \quad (S \cdot K / cm) \quad \text{Eq. 15}$$

Ohmic losses arise from the transport of ions and electrons in the ionic and electronic conducting phases of the composite electrodes and from the transport of ions in the electrolyte. The use of composite electrodes implies to spread the reaction zone over the whole 3D structure of the electrode, this means that the thickness of the electrode is a measure of the path of electrons from current collector to the reaction site and of ions, from the reaction site to the electrolyte in order to be transferred to the anode side. The transport of such charges is affected by several factors, in the following investigation it will be related to observed microscopic properties. Several authors [16,18,21] used particle coordination number in binary random packing of spheres and percolation theory in order to estimate the charge transport properties of composite electrodes. These properties basically include the estimation of effective electronic and ionic resistivities. Originally, the model was proposed by Bouvard et al. [20] and it is based on physical meaningful equations, with reference to a mixture formed by matrix (m-particles) where inclusions are present (m-particles). A scheme of the percolation approach is reported in Figure 29. Using the equations derived by Bouvard et al., it was possible to estimate the effective charge transport properties of the cell's electrodes. The electrolyte ionic resistance was evaluated according to the following equations [36-38] and the experimentally observed thickness. The resistance of multi-layers electrodes was estimated with the use of microscopic observations of Paragraph 3.3 and results proposed by the

percolation theory. The ohmic conductivities relations of pure materials which were used in this analysis were assumed by [15]:

$$\text{Ni: } \sigma_{Ni} = 3.27 \cdot 10^4 - 10.653 \cdot T \quad [S/cm] \quad \text{Eq. 16}$$

$$\text{8YSZ: } \begin{cases} \sigma_{8YSZ} = (3.34 \cdot 10^2) \cdot e^{-\frac{10300}{T}} \quad [S/cm] \\ \sigma_{8YSZ} = 1 / \left( 0.00294 \cdot e^{\left(\frac{10350}{T_{cell}}\right)} \right) \quad [S/cm] \end{cases} \quad \text{Eq. 17}$$

$$\text{LSM: } \sigma_{LSM} = (8.5 \cdot 10^2) \cdot e^{-\frac{1.2810^3}{T}} \quad [S/cm] \quad \text{Eq. 18}$$

In particular it was possible to determine some expressions of electronic and ionic resistivities for the different layers and for different microscopic assessments:

Anode (70% Ni, 30% YSZ; porosity:20%; grain size Ni=2.5  $\mu\text{m}$ ; grain size YSZ=0.5  $\mu\text{m}$ )

$$\begin{aligned} \rho_{e,eff} &= 3.07 \cdot 10^{-4} \cdot e^{-\frac{55634}{T}} \quad \Omega \cdot cm \\ \rho_{ion,eff} &= 2.98 \cdot 10^{-2} \cdot e^{-\frac{10350}{T}} \quad \Omega \cdot cm \end{aligned} \quad \text{Eqs. 19}$$

Anode (50% Ni, 50% YSZ; porosity:10%; grain size Ni=0.5  $\mu\text{m}$ ; grain size YSZ=0.5  $\mu\text{m}$ )

$$\begin{aligned} \rho_{e,eff} &= 1.9 \cdot 10^{-4} \cdot e^{-\frac{55661}{T}} \quad \Omega \cdot cm \\ \rho_{ion,eff} &= 7.1 \cdot 10^{-3} \cdot e^{-\frac{10350}{T}} \quad \Omega \cdot cm \end{aligned} \quad \text{Eqs. 20}$$

Cathode current collecting layer (100% LSM; porosity:30%)

$$\rho_{e,eff} = 1.7 \cdot 10^{-3} \cdot e^{-\frac{1280}{T}} \quad \Omega \cdot cm \quad \text{Eqs. 21}$$

Cathode functional layer (50% LSM, 50% YSZ; porosity:20%; grain size LSM=0.5  $\mu\text{m}$ ; grain size YSZ=0.5  $\mu\text{m}$ ):

$$\begin{aligned} \rho_{e,eff} &= 3.2 \cdot 10^{-3} \cdot e^{-\frac{12798}{T}} \quad \Omega \cdot cm \\ \rho_{ion,eff} &= 7.90 \cdot 10^{-3} \cdot e^{-\frac{10350}{T}} \quad \Omega \cdot cm \end{aligned} \quad \text{Eqs. 22}$$

In **Table 3** it is shown the contribution of each layer to the total cell resistance. A critical layer in the correct cell design seems to be the cathode functional layer (CFL), in fact it affects the charge transfer resistance as well as the ohmic resistance; its contribution is around 45% of total ohmic resistance. The resistance at the interfaces and for contact with current collectors is derived for difference between the estimated value from parameter estimation and the total resistance evaluated through the use of the discussed microscopic model.

The polarization resistance of the cell is plotted as a function of the thickness of the CFL in Figure 31. This polarization resistance includes the charge transfer resistance of the cell as well as the total ohmic resistance previously obtained. Increasing the thickness of the cathode functional layer, a decrease of polarization resistance is observed until reaching a minimum which is different for the investigated operating conditions. After this minimum, the polarization resistance increases as the contribution of the ohmic resistance of the layer increases. According to the simulation, the CFL, of 15  $\mu\text{m}$  thickness, seems to be optimized for operating at around 850  $^{\circ}\text{C}$ . The optimization at lower temperature seems to be achieved with a thicker layer as shown from the curves, in particular at 750 $^{\circ}\text{C}$  the minimum is achieved for a CFL of 17  $\mu\text{m}$  thick. Thus, the electrode seems to be optimized in the range of temperatures between 750-850  $^{\circ}\text{C}$ .

## 5. Conclusions

With the results presented in this paper, we showed how we succeeded coupling microstructural characteristics of the cell electrodes along with the electrical behavior of the same cell. Basically, we have successfully found an approach to use microscopic models along with real data from real cell. The most innovative feature of our work is the use of image analysis techniques for gathering important information of the electrodes microstructure and the task of putting together micromodels already developed for SOFC electrodes not just with microstructural data from literature, but with data taken directly from a real cell. Furthermore, for such an important parameter such as the cathodic resistance of charge transfer, namely  $R_{ct}$ , we proposed a way to extrapolate it from the cell

electrical behavior, again avoiding taking literature values as input for the adopted microscopic models. Finally, we used the models with these effective input data to provide an useful tool to check and predict the performances and the design of a commercial cell. Achieved this task, we have showed how image analysis represents a powerful method not only to analyze the properties of SOFC electrodes, but also to elaborate binary images which can be used to create 3D structure of the electrodes, conserving relevant statistical information of the electrode morphology and topology.

## Acknowledgements

The authors would like to thank Mr. Battista Pernecco of “FN Nuove Tecnologie Servizi Avanzati SpA” and Massimo Agostini of “Centro Ricerche Brasimone—ENEA” for providing the SEM images, CHIMERA®’s software house and its developers (ESSS – Engineering Simulation and Scientific Software Ltda) for the free license of their software.

## 6. Reference

- [1] Malzbender J., Steinbrech R.W., Advanced measurement techniques to characterize thermo-mechanical aspects of solid oxide fuel cells, *Journal of Power Sources* 173 (2007) 60–67.
- [2] Brett D.J.L., Aguiar P., Clague R., Marquis A.J., Schottl S., Simpson R., Brandon N.P., Application of infrared thermal imaging to the study of pellet solid oxide fuel cells, *Journal of Power Sources* 166 (2007) 112–119.
- [3] James R. Wilson, Worawarit Kobsiriphat, Roberto Mendoza, Hsun-Yi Chen, Jon M. Hiller, Dean J. Miller, Katsuyo Thornton, Peter W. Voorhees, Stuart B. Adler & Scott A. Barnett, Three-dimensional reconstruction of a solid-oxide fuel-cell anode, *Nature Materials* 5, 541 - 544 (2006).
- [4] Eric D. Wachsman, Fundamental Mechanisms of SOFC Cathode Reactions, 7th SECA Workshop, 2006.
- [5] Edgar Lara-Curzio, Durability and Reliability of SOFC Materials and Components Durability, 7th SECA Workshop, 2006.
- [6] Bronin D., Stack and cell performance degradation: causes, effects and solutions - the current state of knowledge , REAL SOFC Summer School, September 2-7 Varna, Bulgaria.
- [7] Simwonis D., Tietz F., Stöver D., Nickel coarsening in annealed Ni/8YSZ anode substrates for solid oxides fuel cells, *Solid State Ionics*, Vol. 132, pp. 241-251, 2000.
- [8] K.-R. Lee, S.H. Choi, J. Kim, H.-W. Lee, J.-H. Lee, Viable image analyzing method to characterize the microstructure and the properties of the Ni/YSZ cermet anode of SOFC, *Journal of Power Sources* 140 (2005) 226–234.

- [9] J.-H. Lee a, H. Moon b, H.-W. Lee a, J. Kim a, J.-D. Kim a, K.-H. Yoon b, Quantitative analysis of microstructure and its related electrical property of SOFC anode, Ni-YSZ cermet, *Solid State Ionics* 148 (2002) 15– 26.
- [10] K.-R. Lee a, Y.S. Pyob, B.S. Sob, S.M. Kimb, B.K. Lee b, J.H. Hwang b, J. Kima, J.-H. Lee a, H.-W. Lee, Interpretation of the interconnected microstructure of an NiO-YSZ anode composite for solid oxide fuel cells via impedance spectroscopy, *Journal of Power Sources* 158 (2006) 45–51
- [11] Bhavani V. Kasula (a), Leslie Mercado(a), Pietro Asinari (b), and Michael R. von Spakovsky, 3D microstructure reconstructions of solid oxide and proton exchange membrane fuel cell electrodes with application to numerical simulations of reacting mixture flows using LBM, *Proceedings of IMECE 2007 2007 ASME International Mechanical Engineering Congress and Exposition* November 12-15, 2007 Seattle, Washington.
- [12] Tanner C.W., Fung K.-Z., Virkar A.V., The effect of porous composite electrode structure on solid oxide fuel cell performance, *J. of Electrochemical Society* 144, N°1 (1997) 21–30.
- [13] Virkar A.V., Chen J., Tanner C.W., Kim J.W., The role of electrode microstructure on activation and concentration polarizations in solid oxide fuel cells, *Solid State Ionics* 131, (2000) 189-198.
- [14] Kenjo T., Osawa S., Fujikawa K., High temperature air cathodes containing ion conductive oxides, *J. of Electrochemical Society* 138, N°2 (1991) 349–355.
- [15] Jeon D.H., Nam J.H., Kim C.J., Microstructural Optimization of Anode-Supported Solid Oxide Fuel Cells by a Comprehensive Microscale Model, *Journal of The Electrochemical Society*, 153 (2) A406-A417 (2006).
- [16] Nam J.H., Jeon D.H., A comprehensive micro-scale model for transport and reaction in intermediate temperature solid oxide fuel cells, *Electrochimica Acta*, Vol.51, pp. 3446-3460, 2006.
- [17] Costamagna P., Costa P., Antonucci V., Micro-modelling of solid oxide fuel cell electrodes, *Electrochimica Acta*, Vol.43, No° 3-4, pp. 375-394, 1998.
- [18] Costamagna P., Panizza M., Cerisola G., Barbucci A., Effect of composition on the performance of cermet electrodes. Experimental and theoretical approach, *Electrochimica Acta*, Vol.47, pp. 1079-1089, 2002.
- [19] Barbucci A., Carpanese P., Cerisola G., Viviani M., Electrochemical investigation of mixed ionic/electronic cathodes for SOFCs, *Solid State Ionics* 176 (2005) 1753-1758.
- [20] Bouvard D., Lange F.F., *Acta Metall. Mater.* 39 (1991), 3083.
- [21] Scheiner L.C.R., Martin C.L., Bouvard D., Bultel Y., Modelling of the electrochemical performance of different types of fuel cell electrodes by discrete simulations, *Proceedings of the Second European Fuel Cell Technology and Applications Conference, EFC2007*, December 11-14, 2007, Rome Italy.
- [22] Asinari P., Calì M., von Spakovsky M.R., Kasula B.V., Direct numerical calculation of the kinematic tortuosity of reactive mixture flow in the anode layer of solid oxide fuel cells by the lattice Boltzmann method, *Journal of Power Sources* Volume: 170, Issue: 2, July 10, 2007, pp. 359-375.
- [23] P. M. Adler, C. G. Jacquin, J. A. Quiblier, Flow in simulated porous media, *International Journal of Multiphase Flow*, Volume 16, Issue 4, July-August 1990, Pages 691-712
- [24] <http://www.chimera4.com.br> – CHIMERA 4.1 User manual & Scientific manual
- [25] Leone P, Asinari P, Santarelli M., Borchiellini R., Calì M., Experimental investigations of the microscopic features and polarization limiting factors of planar SOFCs with LSM and LSCF cathodes, *J. Power Sources* V. 177 (2008), 111-122..
- [26] Haanappel V.A.C, Smith M.J., A review of standardising SOFC measurement and quality assurance at FZJ, *Journal of Power Sources* 171 (2007) 169–178.
- [27] Lanzini A., Leone P., M. Santarelli, P. Asinari, M. Calì, R. Borchiellini Performances and degradation phenomena of solid oxide anode-supported cells with LSM and LSCF cathodes: an experimental assessment, accepted on April 15th 2008 on the ASME, *J. of fuel cells science and technology*.

- [28] Jacques A. Quiblier, A new three-dimensional modeling technique for studying porous media, *Journal of Colloid and Interface Science*, Volume 98, Issue 1, March 1984, Pages 84-102
- [29] P. NIKOLOPOULOS and D. SOTIROPOULOU, *J. Mater.Sci. Lett.* 6 (1996) 1429.
- [30] A. TSOGA, A. NAOMIDIS and P. NIKOLOPOULOS, *Acta mater.* 44 (1996) 3679.
- [31] JIANG S.P., CHAN S.H., A review of anode materials development in solid oxide fuel cells, *Journal of Materials Science* 39 (2004) 4405 – 4439
- [32] T. Iwata, Characterization of Ni-YSZ anode degradation for substrate-Type solid oxide fuel cells, *J. Electrochemical society*, V.143, pp.1521-1525, 1996.
- [33] S. Primdahl, M. Mogensen., Durability and thermal cycling of Ni/YSZ cermet anodes for solid oxide fuel cells, *Journal of Applied Electrochemistry*, V. 30, Issue 2, pp 247-257, 2000
- [34] Noren D.A. et Al, Clarifying the Butler–Volmer equation and related approximations for calculating activation losses in solid oxide fuel cell models, *J. of Power Sources* 152 (2005) 175–181.
- [35] Zhao F., Virkar A. V., Dependence of polarization in anode-supported solid oxide fuel cells on various cell parameters, *Journal of Power Sources* 141 (2005) 79–95.
- [36] Costamagna P. et Al., Modeling of Solid Oxide Heat Exchanger Integrated Stacks and Simulation at high Fuel Utilization, *J. Electrochemical Soc.*, Vol. 145 (11), pp. 3995-4006 (1998).
- [37] Baozhen L. et Al., Solid Oxide Fuel Cell operable over wide temperature range, US Patent n°6,207,311 B1, Inventors Assigne: Siemens Westinghouse Power Corporation, 27/3/2001.
- [38] F. Bessette II et Al., A Mathematical Model of a Solid Oxide Fuel Cell, *J. Electrochemical Society*, V.142, pp. 3792-3800, 1995.
- [39] Z.R. Liang, C.P. Fernandes, F.S. Magnani, P.C. Philippi, A reconstruction technique for three-dimensional porous media using image analysis and Fourier transforms, *Journal of Petroleum Science and Engineering* 21 (1998) 273–283.

## LIST OF SYMBOLS

<i>ASR</i>	Area Specific Resistance ( $\Omega \text{ cm}^2$ )	$V_{Nernst}$	Nernst potential (V)
<i>F</i>	Faraday number ( $\text{C mol}^{-1}$ )	<i>YSZ</i>	Yttria Stabilized Zirconia
$i_{as}$	Anode limiting current ( $\text{A cm}^{-2}$ )	$Z(x)$	Phase function
$i_{cs}$	Cathode limiting current ( $\text{A cm}^{-2}$ )	$C(u)$	Correlation function
$i$	Cell current density ( $\text{A cm}^{-2}$ )	$R(u)$	Spatial autocorrelation function
<i>LSCF</i>	Lanthanum Strontium Cobalt Ferrite Oxide	$x$	Spatial coordinate in the image-plane
		$u$	Random spatial dislocation in the image-plane
<i>LSM</i>	Lanthanum Strontium Manganese Oxide		
<i>LBM</i>	Lattice Boltzmann Model		
$n$	number density of molecules in the mixture		
$OCV_{exp}$	Open Circuit Voltage (V)	<i>Greek</i>	
$R$	universal gas constant ( $\text{J mol}^{-1} \text{ K}^{-1}$ )	$\alpha$	effective charge transfer coefficient
$R_{ct}$	Intrinsic charge transfer resistance ( $\Omega \text{ cm}^2$ )	$\phi$	electrode porosity function
$R_{ct}^{eff}$	Effective charge transfer resistance ( $\Omega \text{ cm}^2$ )	$\rho$	Material electrical resistivity
$R_p$	Polarization resistance ( $\Omega \text{ cm}^2$ )	$\sigma$	Material electrical conductivity
$R_{YSZ}$	Ohmic electrolyte resistance ( $\Omega \text{ cm}^2$ )		
$R_{\Omega}$	Cell ohmic resistance ( $\Omega \text{ cm}^2$ )	$\Gamma$	Electrode phase
<i>SOFC</i>	Solid Oxide Fuel Cell		
$T$	temperature (K)		
$V_c$	Cell terminal voltage (V)		



# TABLES

## IMAGE ANALYSIS METHODOLOGY

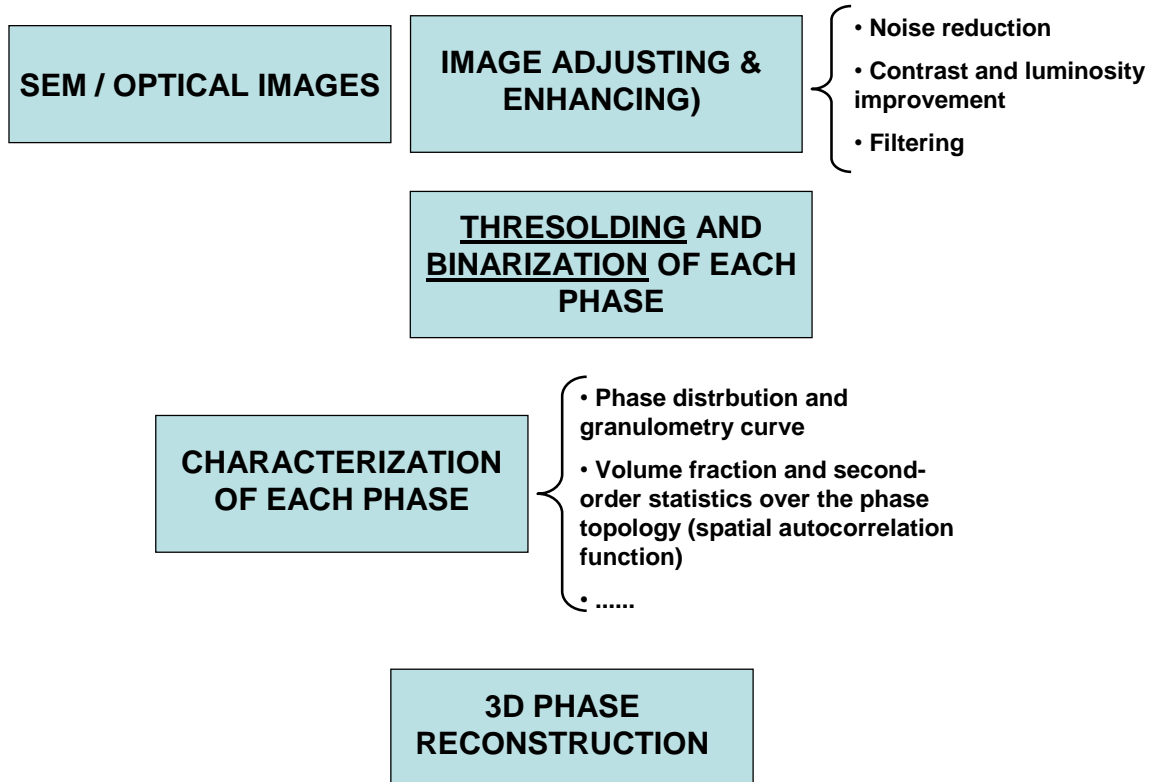


Table 1. Steps for image analysis

---



---

**IMAGE ANALYSIS - MICROSTRUCTURAL RESULTS**

---

IMAGE TYPE	POROSITY [%]	VOL. Electronic Phase* [%]	VOL. Ionic Phase** [%]	GRAIN SIZE Electronic Ph.* [μm]	GRAIN SIZE Ionic Ph.** [μm]	Thickness [μm]
ASC1 SEM-BSE / ANODE SUPPORT (Fig. 5)	26	45	29	0,5	0,8	520
ASC1 SEM / ANODE SUPPORT (Fig. 1)	25	44	31	0,5	0,8	-
ASC1 SEM-BSE / CATHODE ACTIVE LAYER (Fig. 24)	7	48	45	0,5	0,6	14
ASC1 SEM-BSE / CATHODE COLLECTOR LAYER (Fig. 24)	30	70	0	1	-	18
OPERATED ASC1 - OPTICAL (Fig. 21)	32	34	34	1	0,8	-

\* **Ni** for the anode electrode and **LSM** for the cathode layers

\*\* **YSZ** for both electrodes

---

Table 2. Microstructural characterization of ASC1 composite electrodes

Temperature (°C)	Contribution to total ohmic %		Contribution to total ohmic %		Contribution to total ohmic %	
	750	800	800	850	850	850
Ohmic total parameter estimation (ohm cm <sup>2</sup> )	3.2E-01	1.9E-01		1.4E-01		
Electrolyte (ohm cm <sup>2</sup> )	4.0E-02	12.5	2.3E-02	12.0	1.6E-02	11.9
Anode Functional Layer (ohm cm <sup>2</sup> )	3.4E-02	10.7	1.9E-02	10.3	1.4E-02	10.1
Anode Current Collecting Layer (ohm cm <sup>2</sup> )	7.5E-06	0.0	7.7E-06	0.0	7.8E-06	0.0
Cathode Functional Layer (ohm cm <sup>2</sup> )	1.5E-01	45.5	8.3E-02	43.8	5.9E-02	43.3
Cathode Cathode Collecting Layer (ohm cm <sup>2</sup> )	1.3E-05	0.0	1.2E-05	0.0	1.2E-05	0.0
Total arising from cell (ohm cm <sup>2</sup> )	2.2E-01	68.7	1.2E-01	66.1	8.8E-02	65.4
Interfaces and contact resistance (ohm cm <sup>2</sup> )	1.0E-01	31.3	6.4E-02	33.9	4.7E-02	34.6

Table 3. Contribution of each cell's layer to the total ohmic resistance

# FIGURES

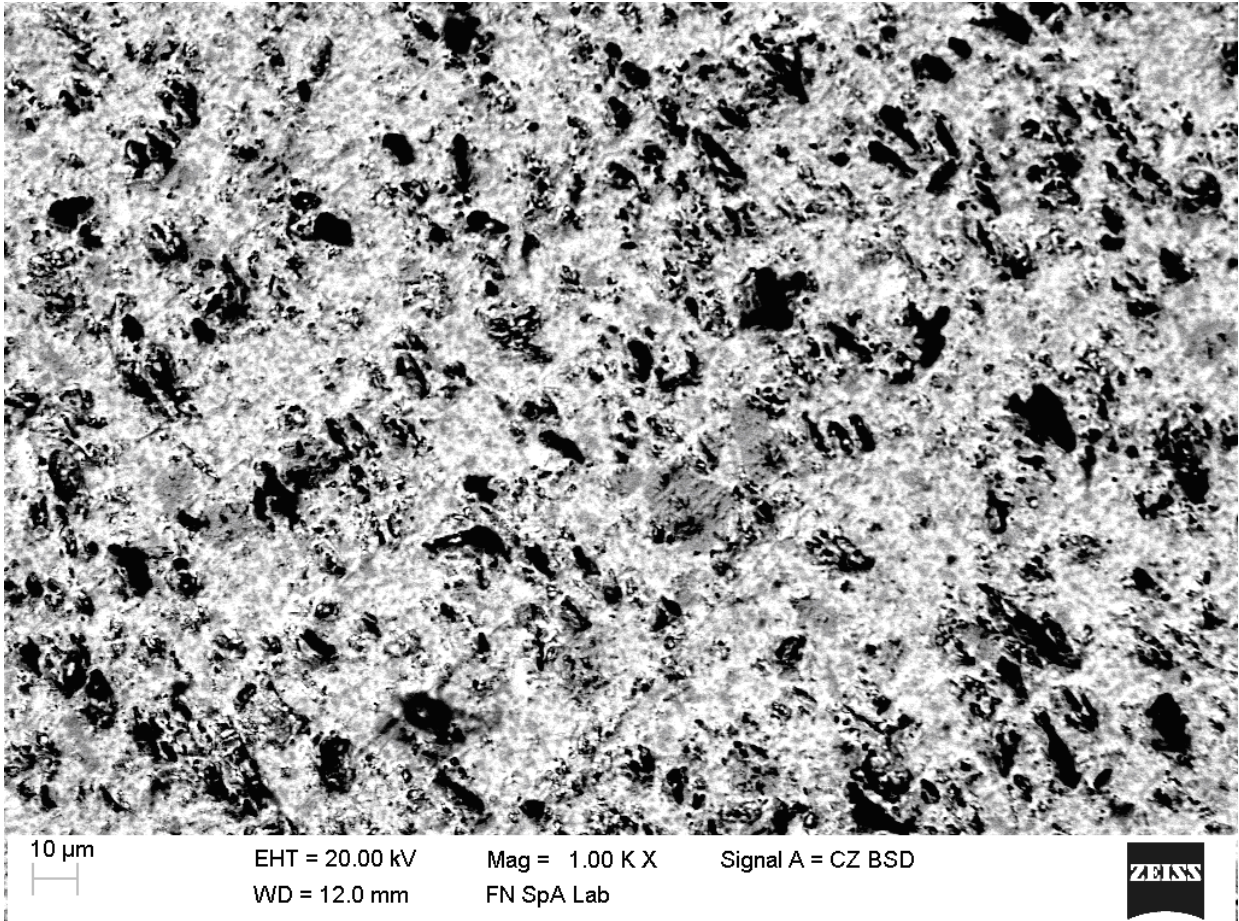


Figure 1. SEM Image of ASC1 anode support after the step of image adjusting and enhancing

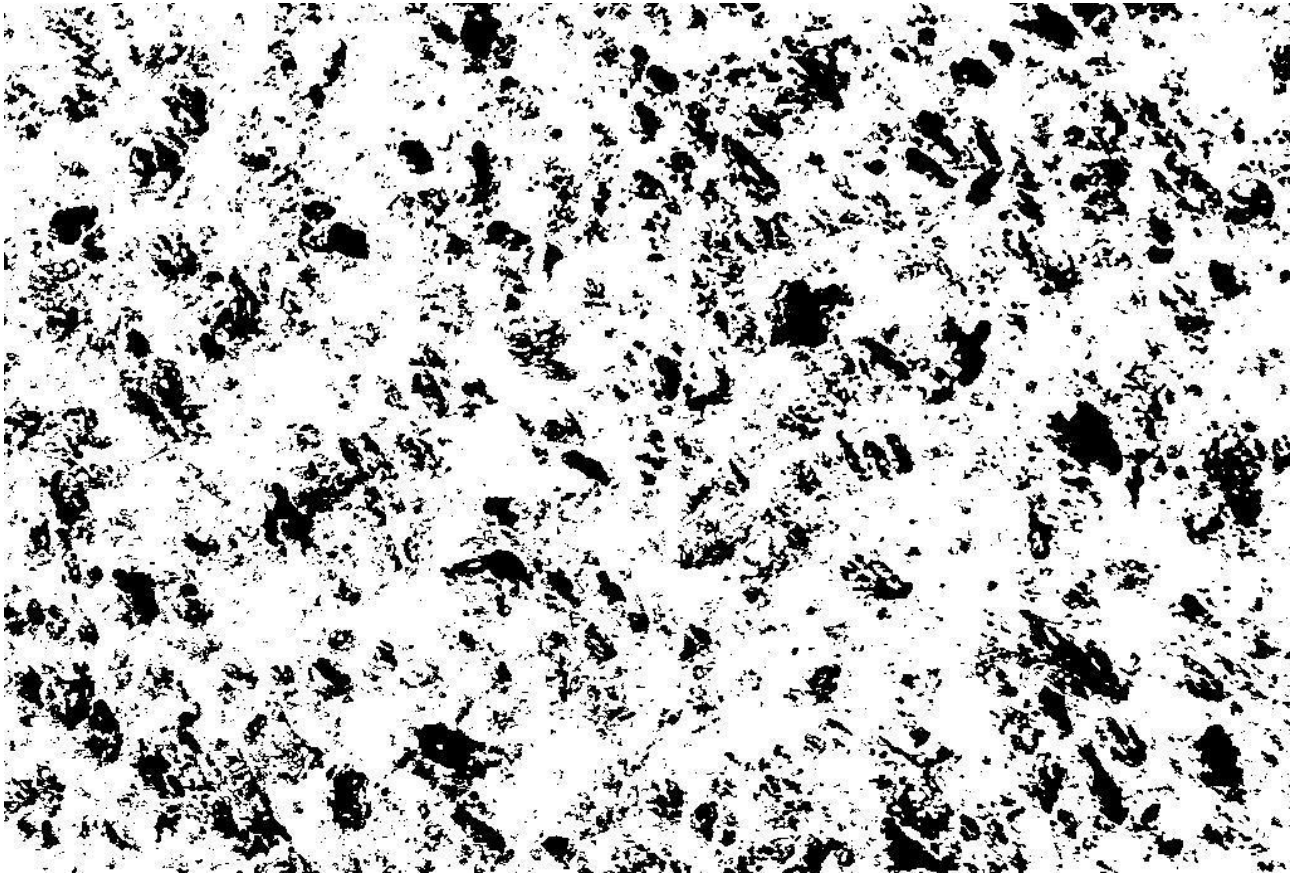


Figure 2 - Binary image of the pores phase of image of Figure 1

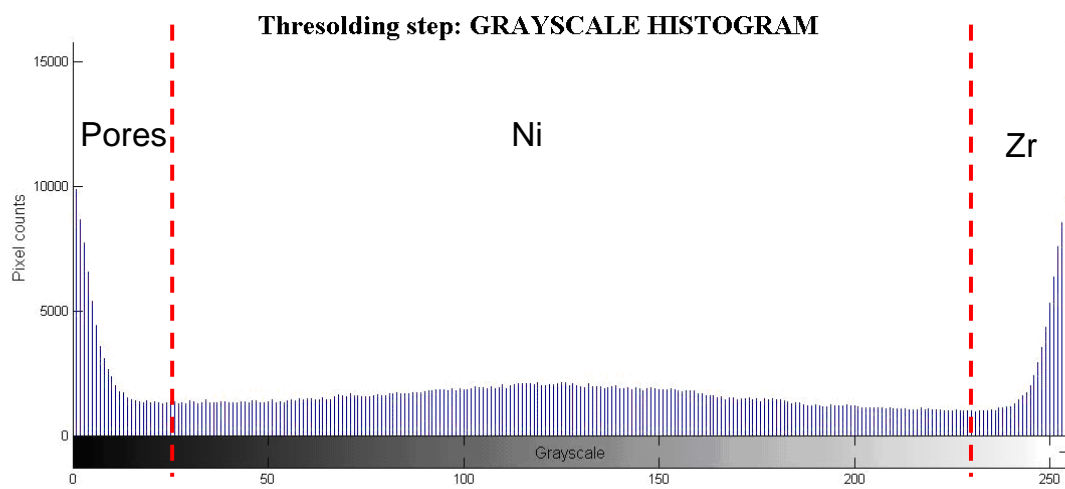


Figure 3 – Grayscale histogram shaping of the anode image reported in figure x



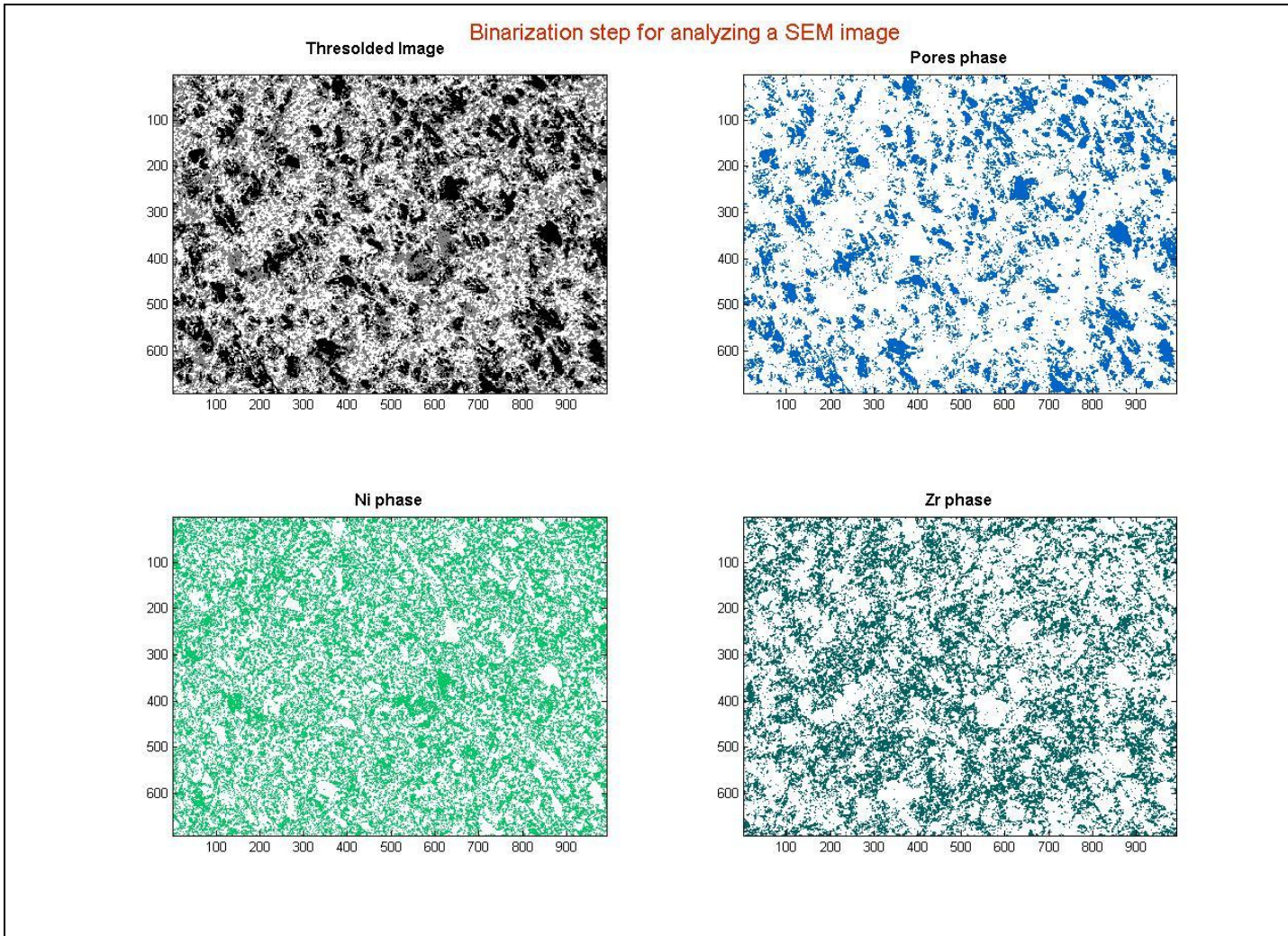


Figure 4 – Binarized images of each phase present in figure x

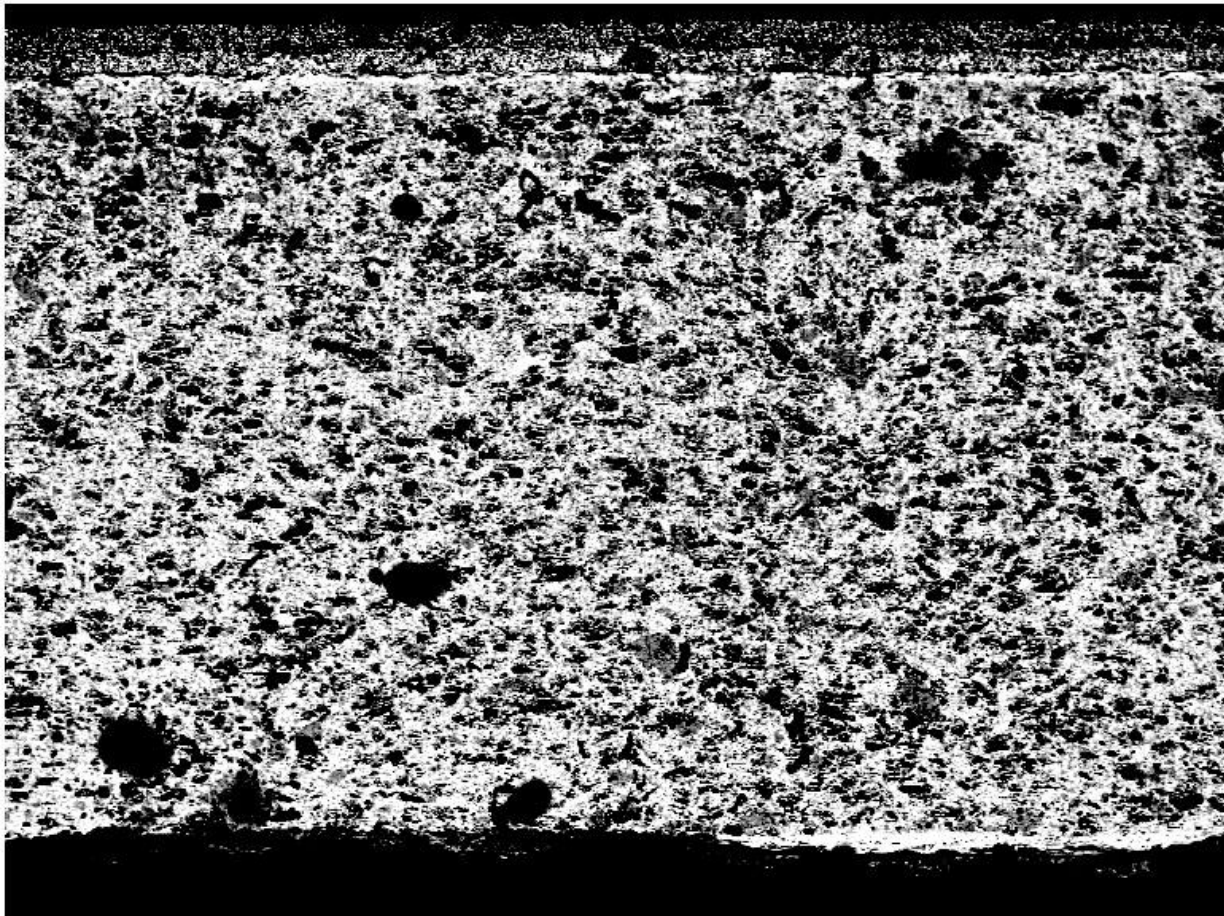
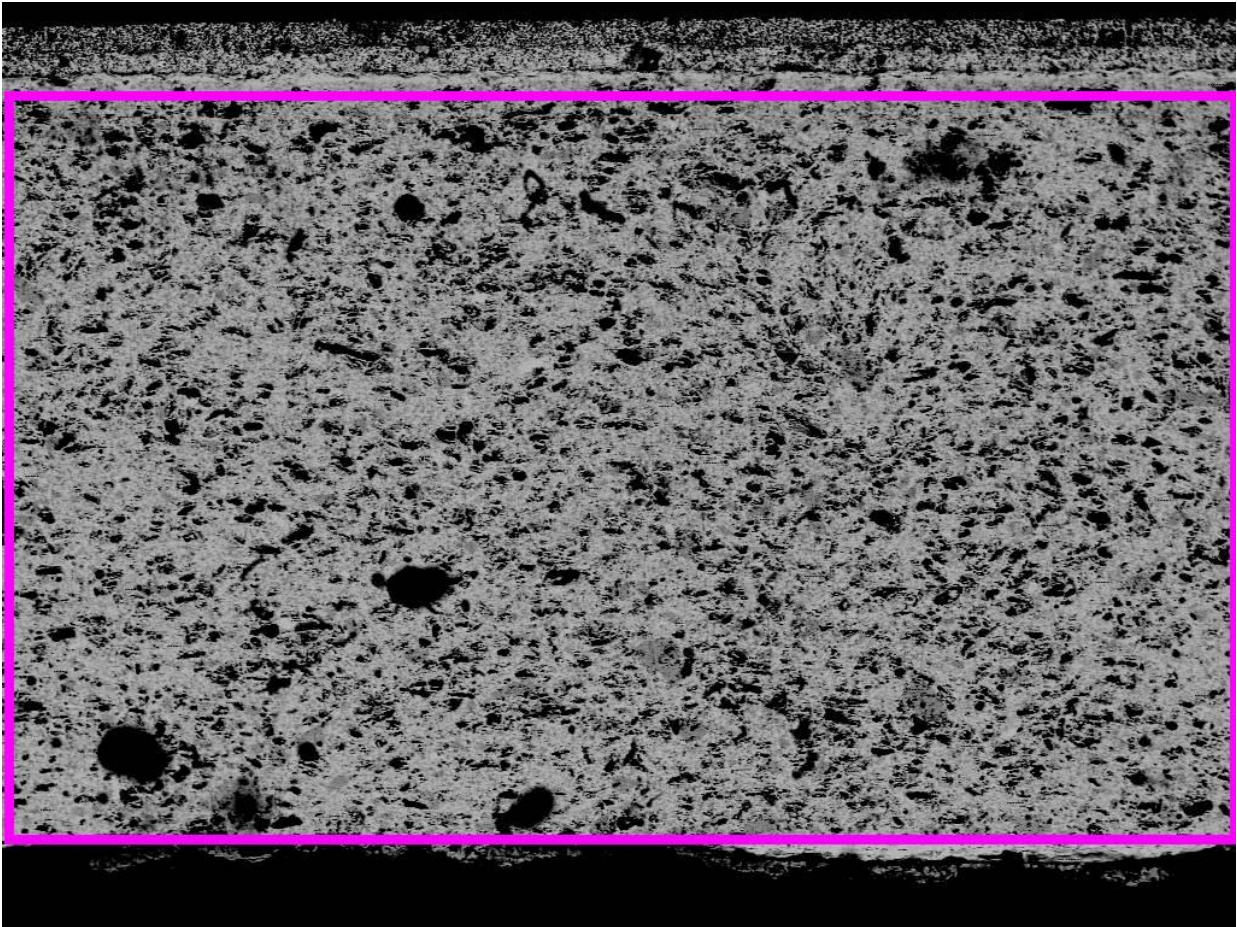


Figure 5. SEM back-scattering image of the entire section of an ASC1 cell (from bottom to top: anode support, YSZ electrolyte, cathode active layer and current collector layer)





400µm

Electron Image 1

Figure 6. Top) SEM BSE image of whole cell section



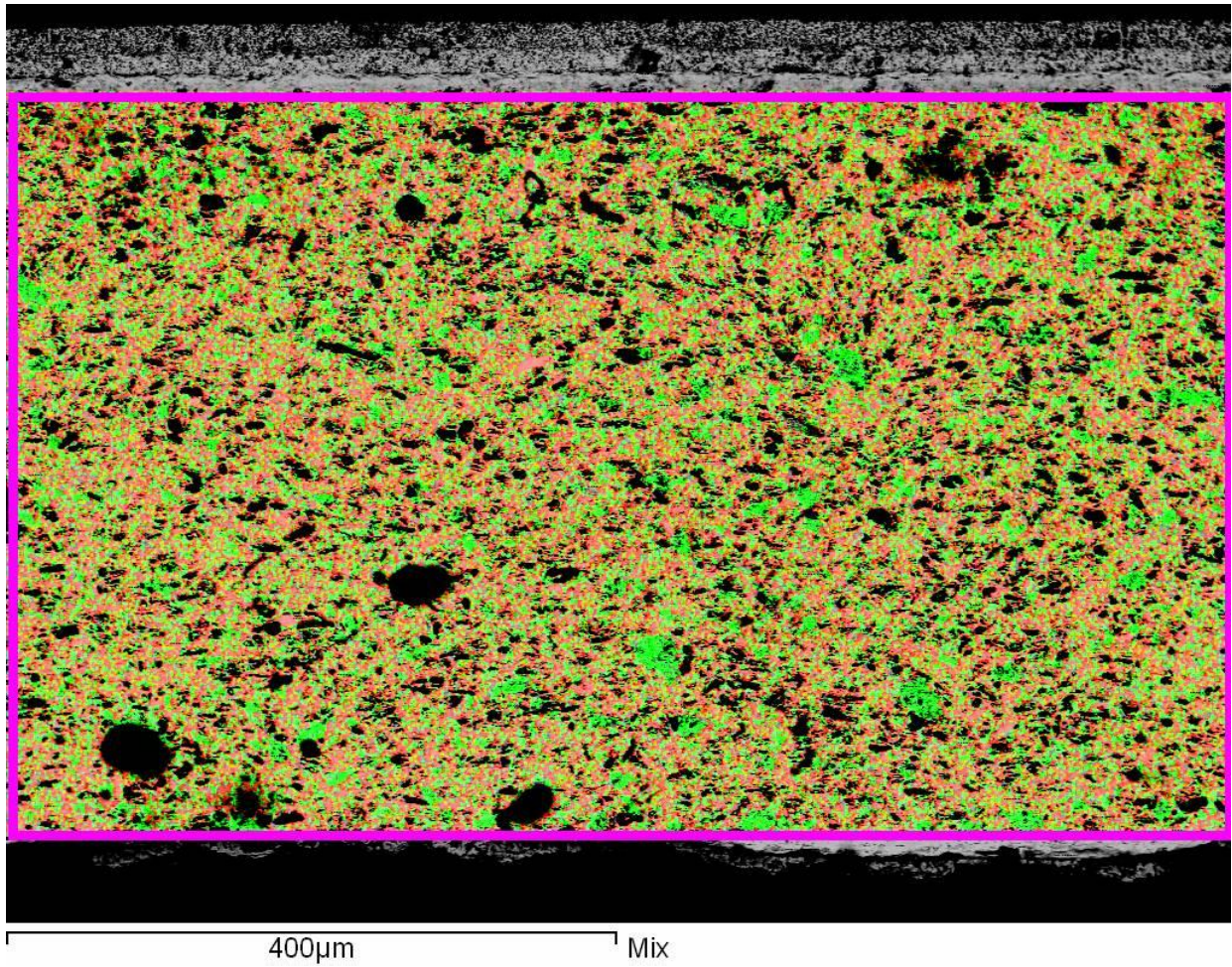


Figure 7. EDS mapping of Ni (green) and Zr (red)

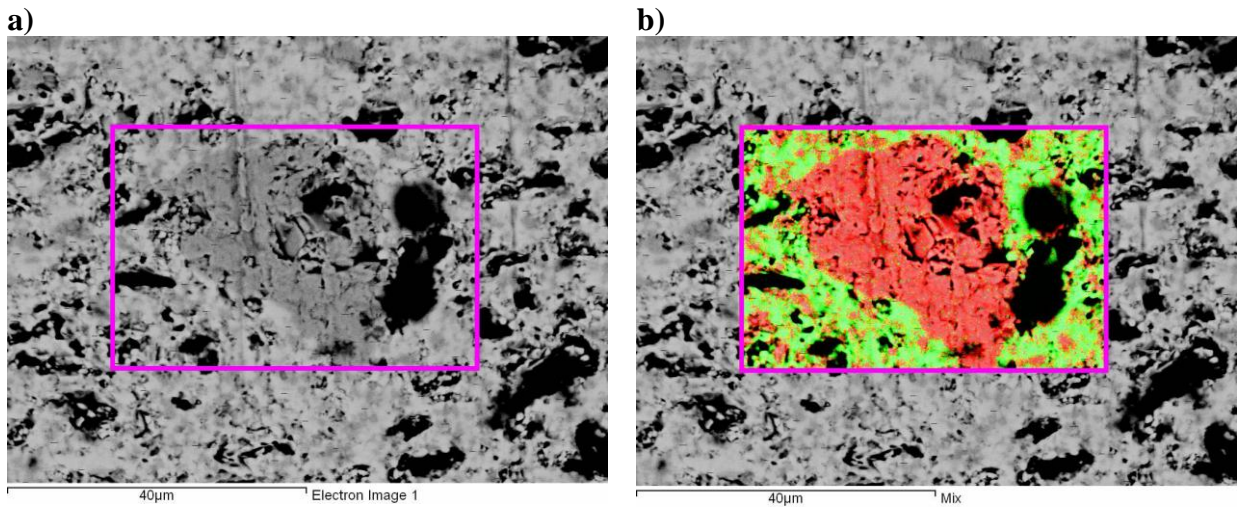


Figure 8. a) SEM BSE image of selected region for EDS mapping; b) EDS element mapping of selected region (Red: Ni, Green: Zr).

### Pores Granulometry of selected images

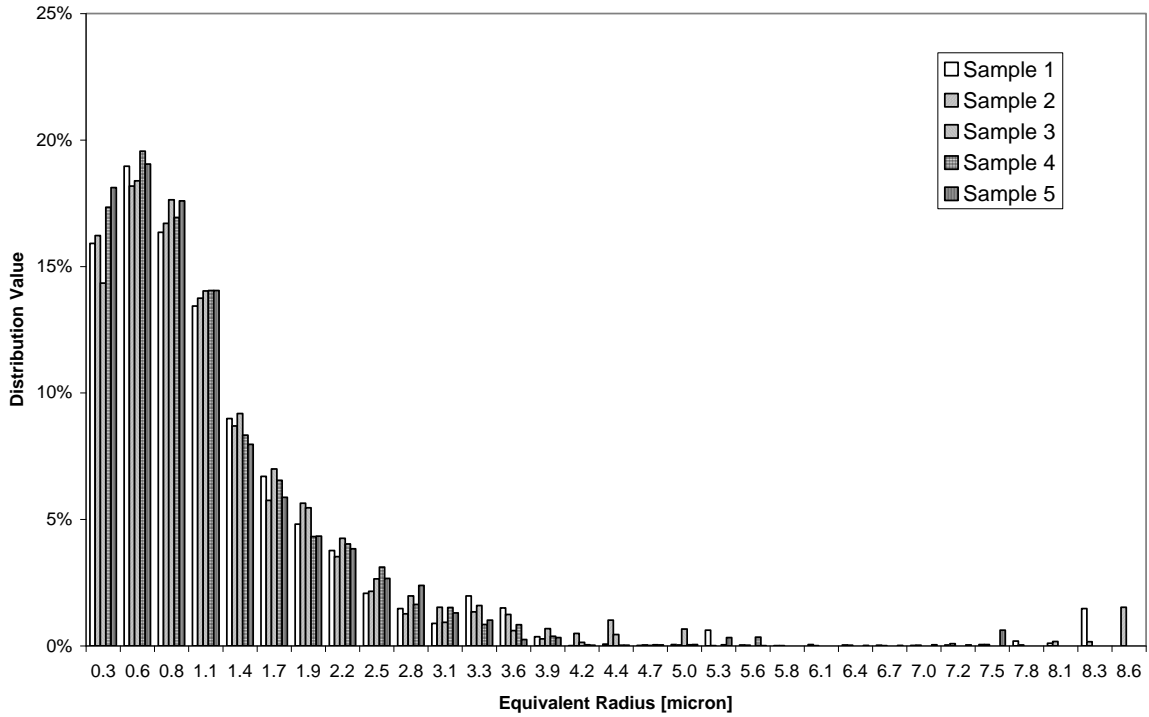


Figure 9 – Comparison of pores distribution from 5 samples of ASC1 anode support

### ASC1 ANODE SUPPORT: AVERAGE PORES DISTRIBUTION

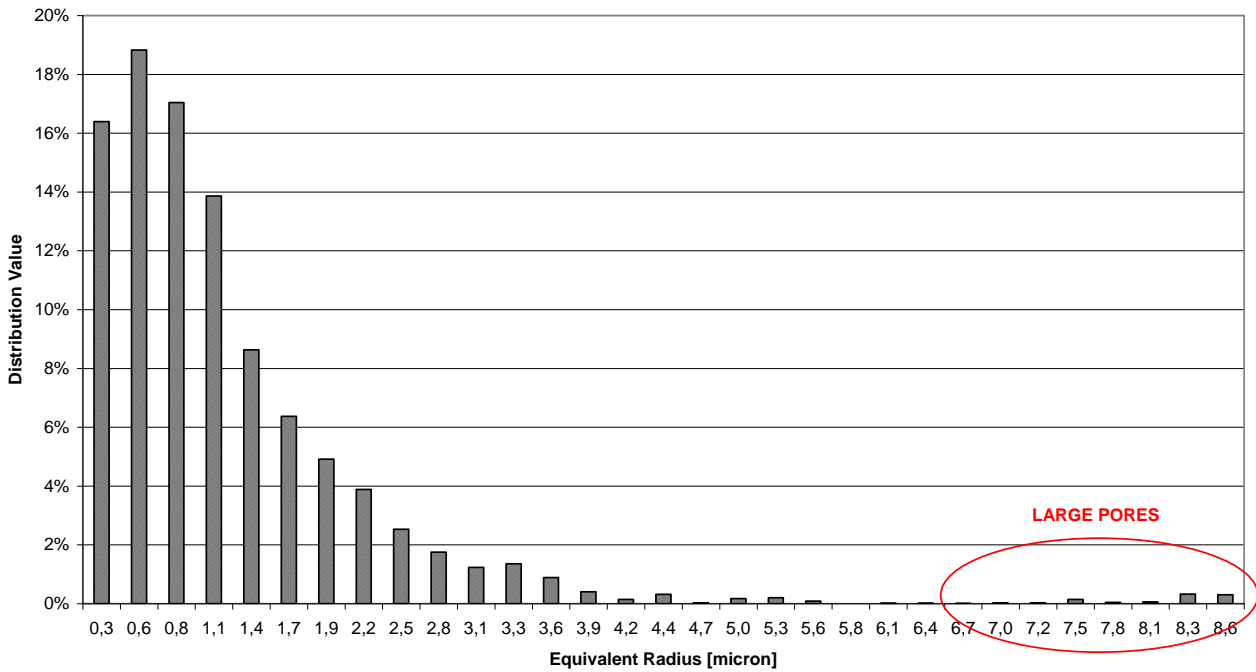


Figure 10 – Average pores' distribution for an ASC1 anode support

### Ni Granulometry of selected images

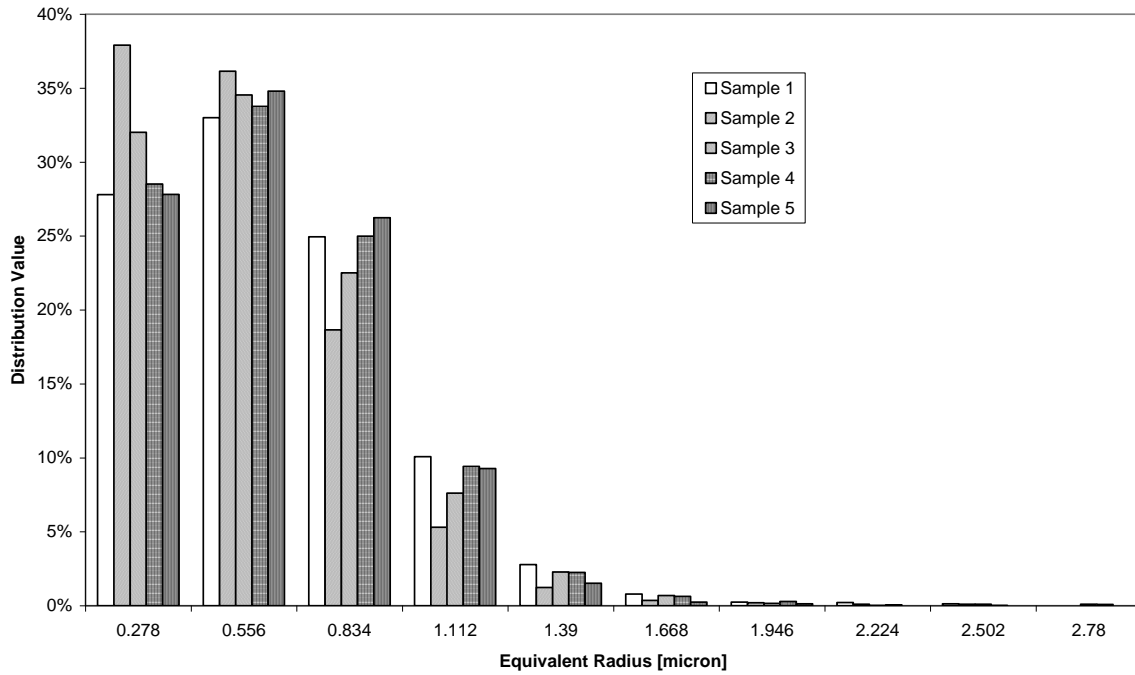


Figure 11 – Comparison of Ni distribution from 5 samples of ASC1 anode support

### ASC1 ANODE SUPPORT: AVERAGE Ni DISTRIBUTION

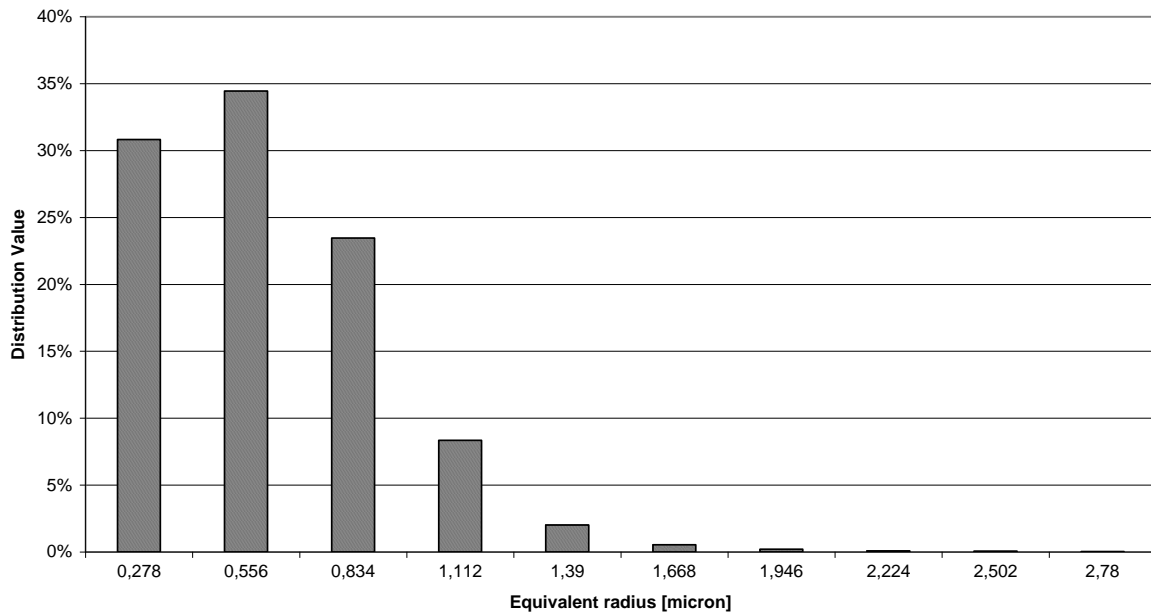


Figure 12 – Average Ni distribution for an ASC1 anode support

## ASC1 ANODE SUPPORT: AVERAGE PHASES DISTRIBUTION

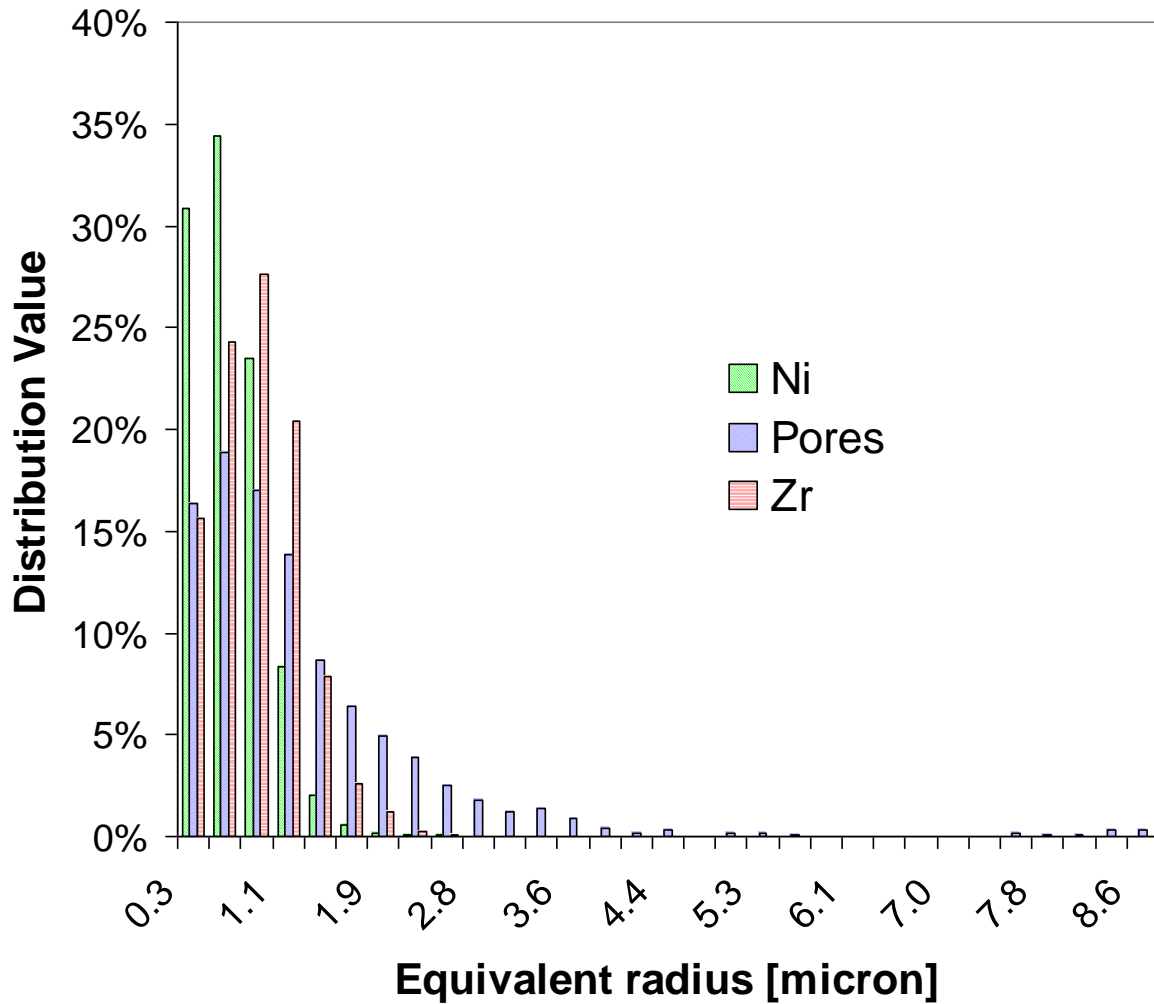


Figure 13 – Average phases distributions for an ASC1 anode support

### "Ni" phase - Spatial correlation function

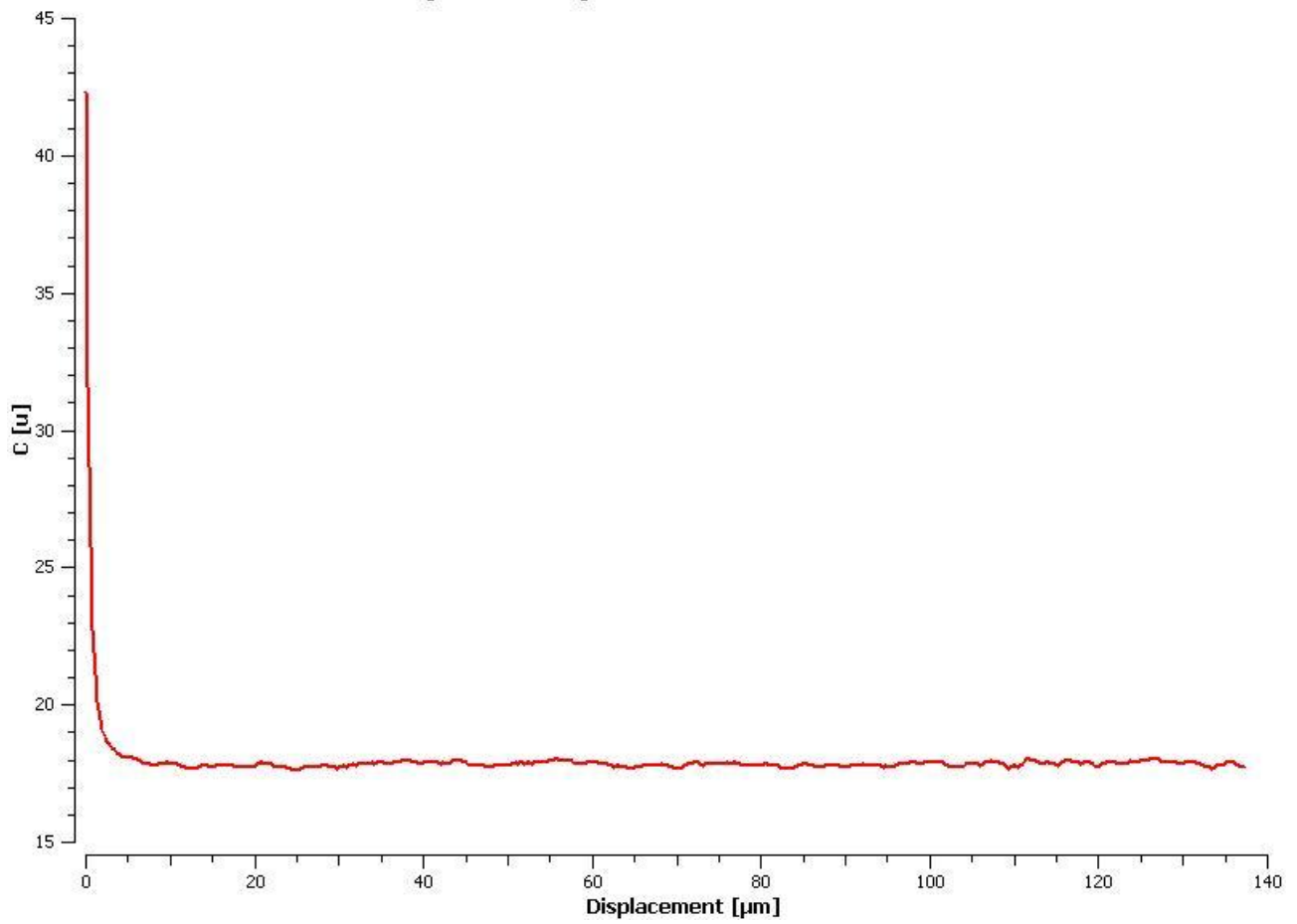


Figure 14 – "Ni" phase spatial autocorrelation function



### "Zr" phase - Spatial correlation function

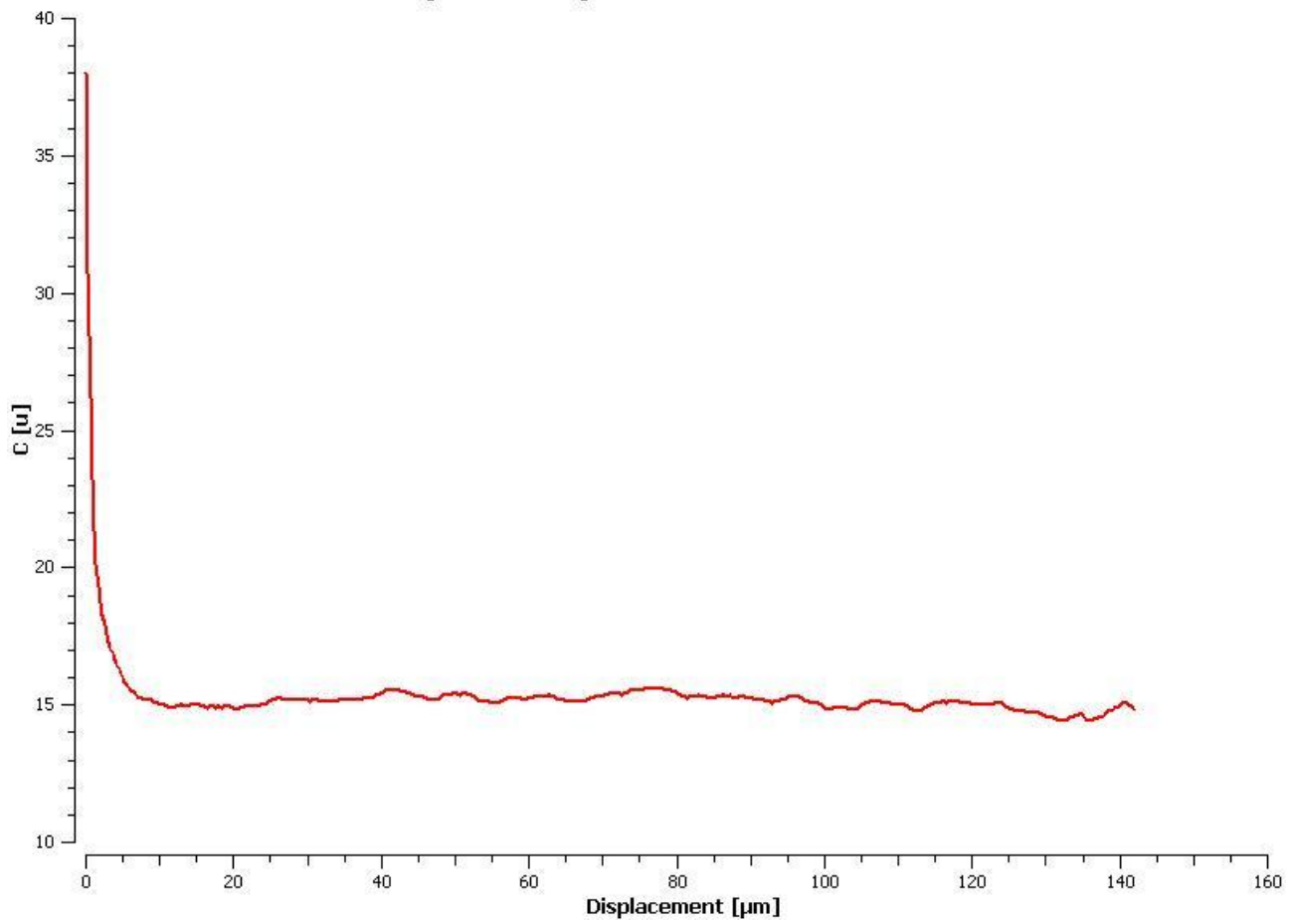


Figure 15 – “Ni” phase spatial autocorrelation function

### "Pores" phase - Spatial correlation

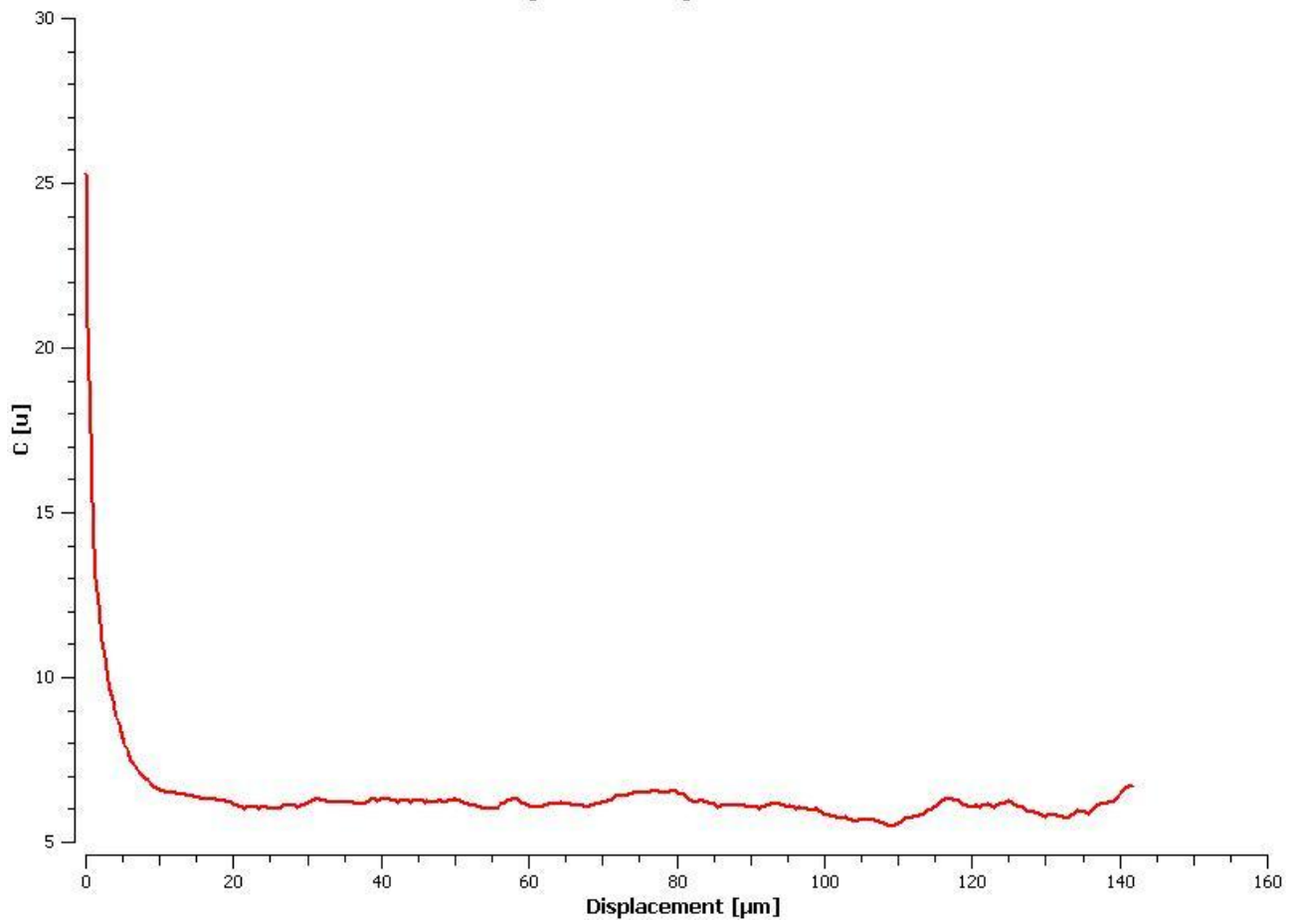


Figure 16 – “Pores” phase spatial autocorrelation function

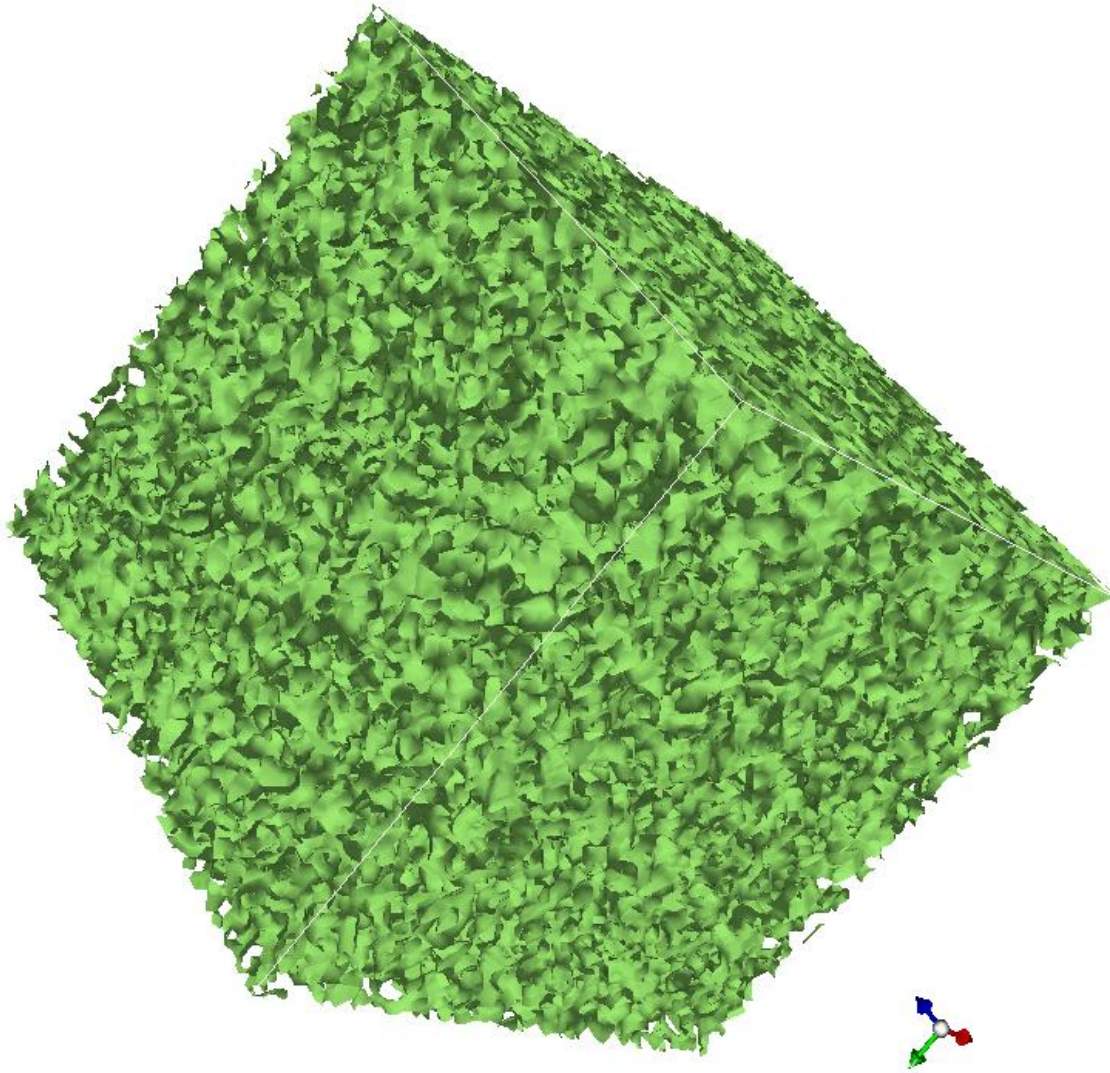


Figura 17- Ni phase 3D reconstruction (cube  $27.8 \times 27.8 \times 27.8 \mu\text{m}^3$ )



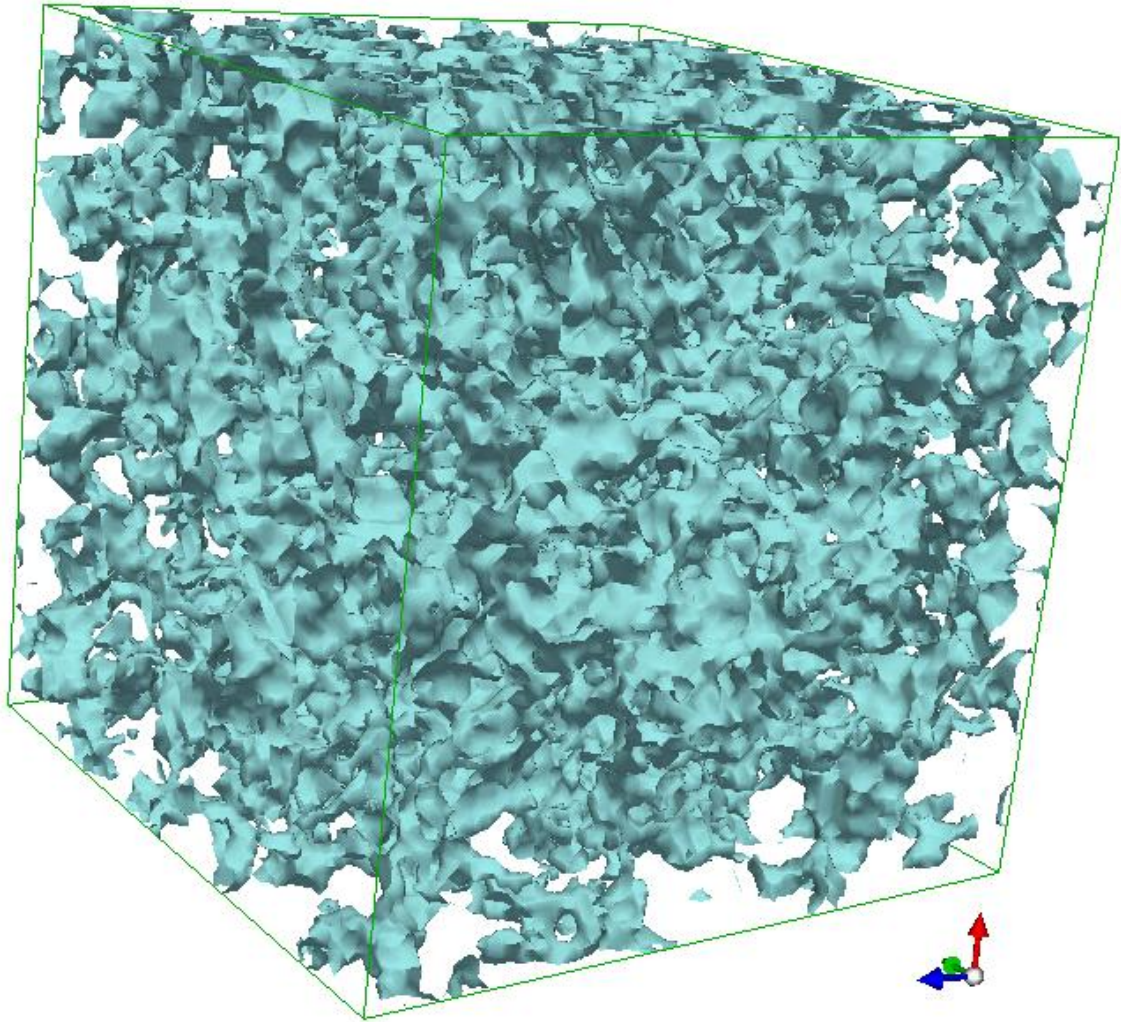


Figure 18 – Pores phase 3D reconstruction (cube  $27.8 \times 27.8 \times 27.8 \mu\text{m}^3$ )



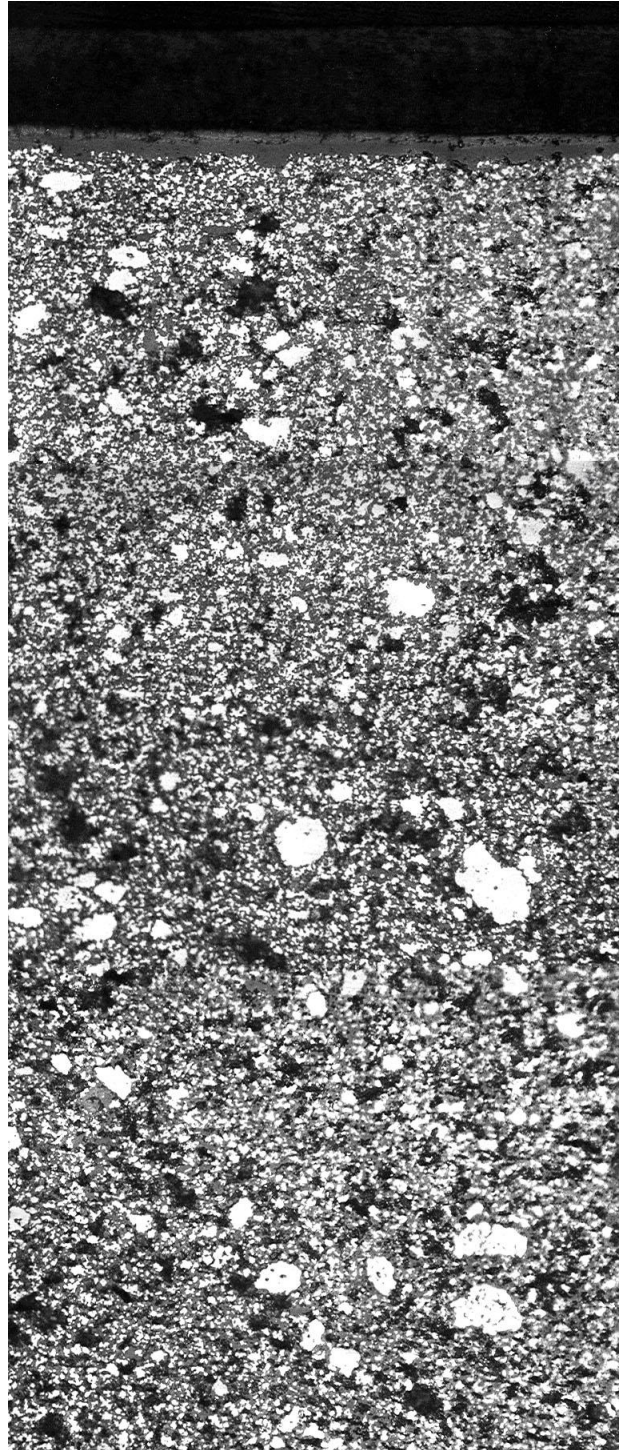
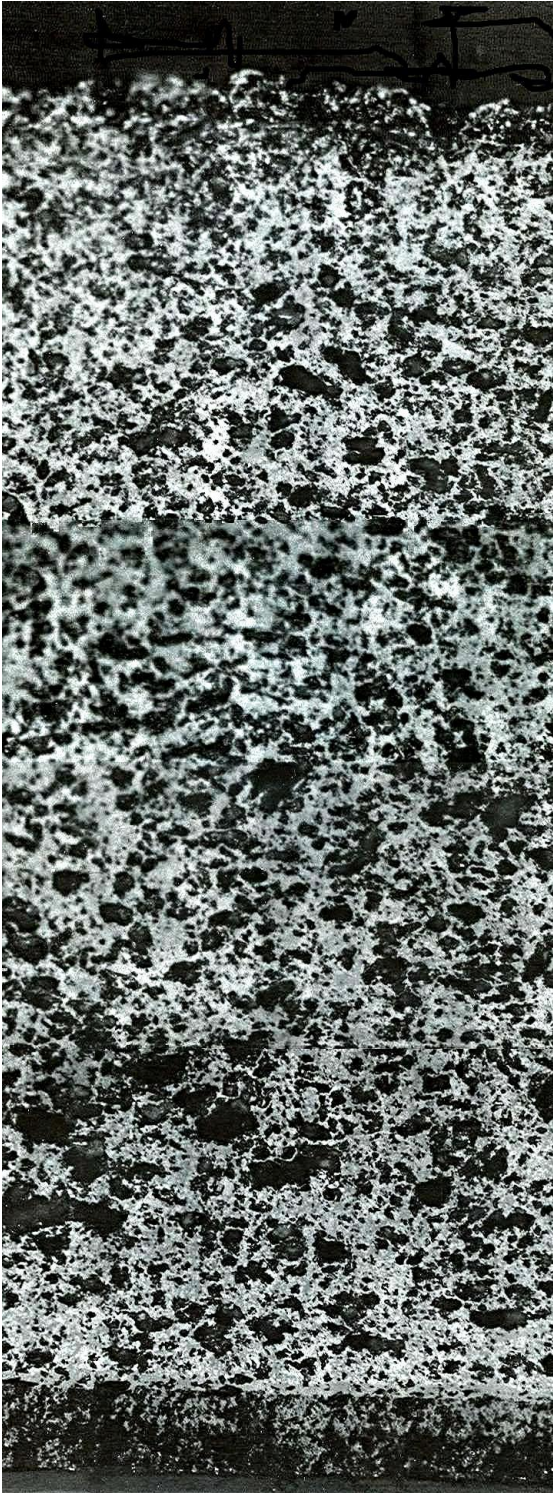


Figure 19 – Cross section of an ASC1 anode support before (left) and after (right) testing.

## Anode support: Ni-phase granulometry before and after cell testing

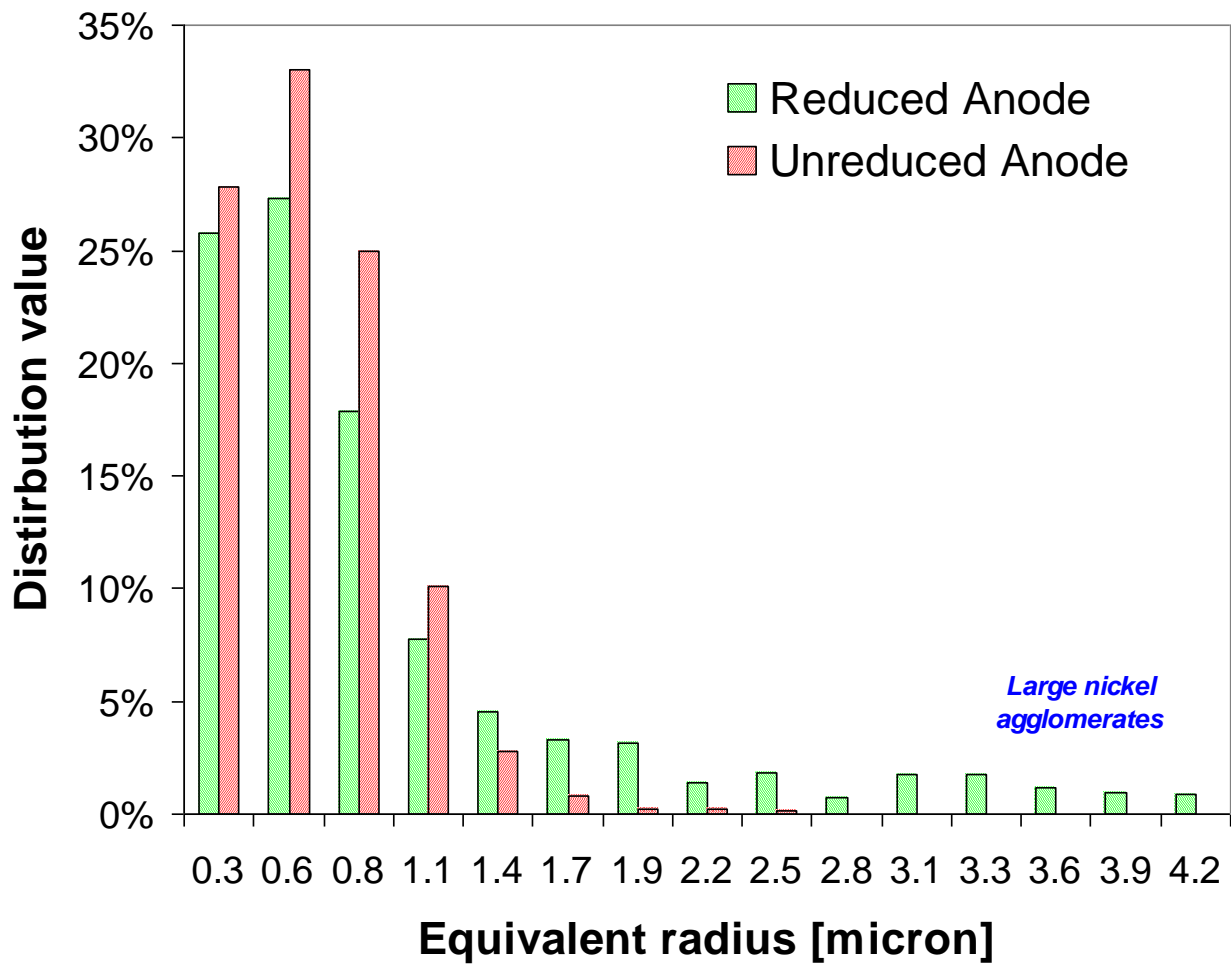


Figure 20. Comparison of Ni-phase granulometry in a ASC1 cell before and after testing



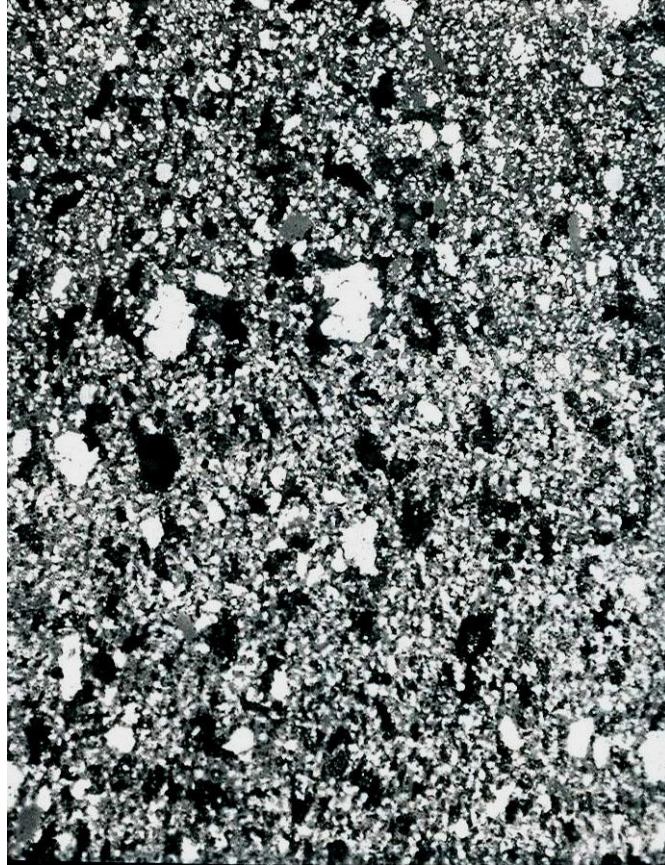


Figure 21 – Optical image of an operated anode: Ni agglomeration occurred with large white “islands” of Ni clearly visible

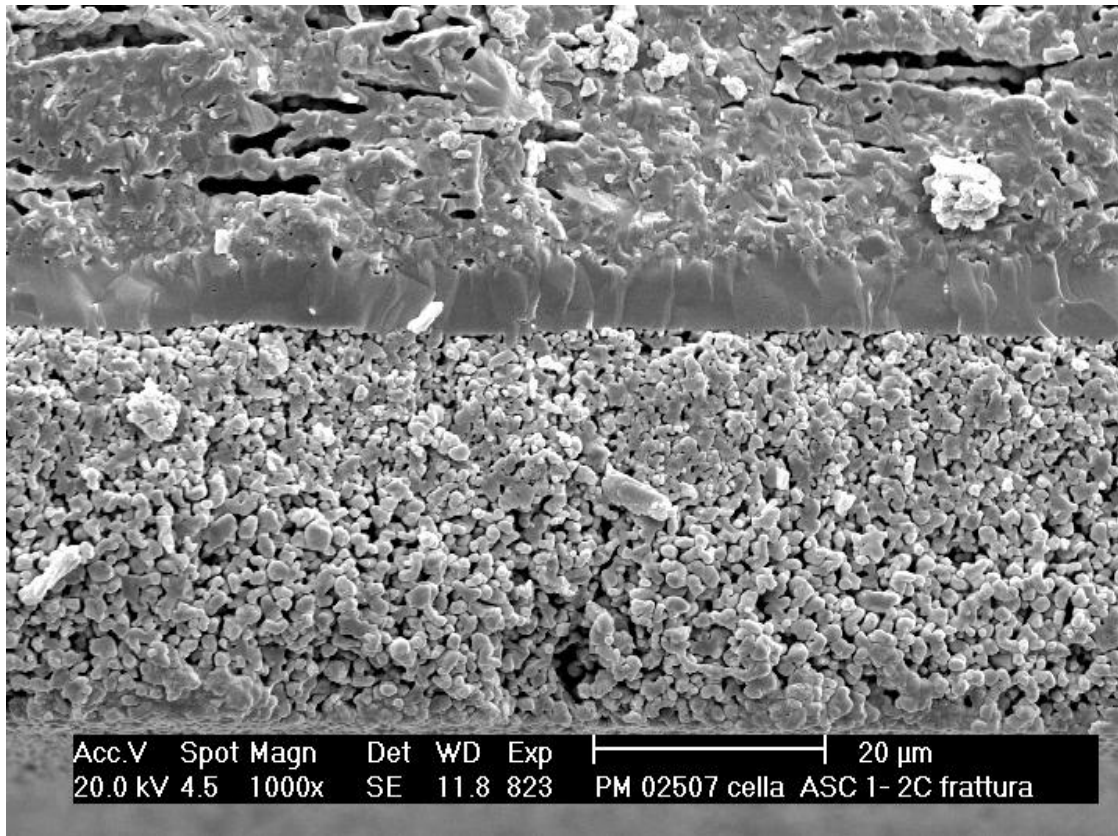


Figure 22. SEM image of the ASC1 cell (from top to bottom: Ni/8YSZ anode support, 8YSZ dense electrolyte, LSM/8YSZ active layer, LSM porous current collector layer)

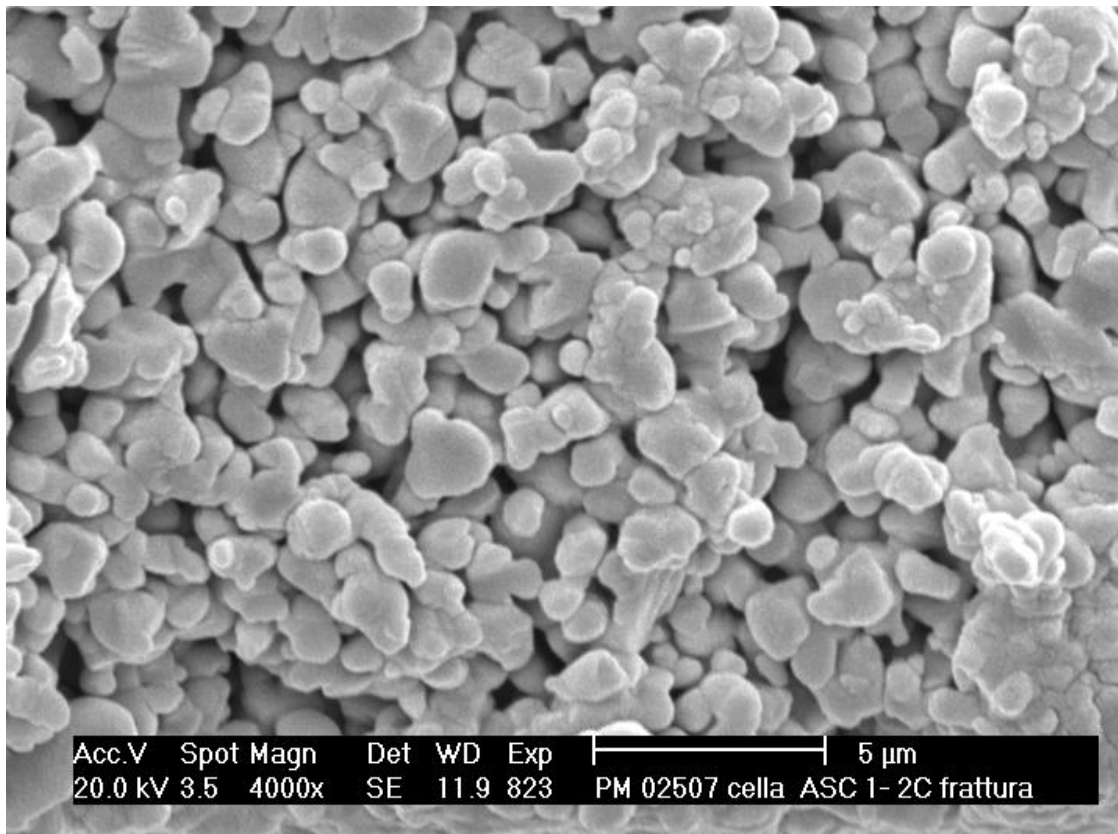




Figure 23. SEM image of the cathode current collector layer

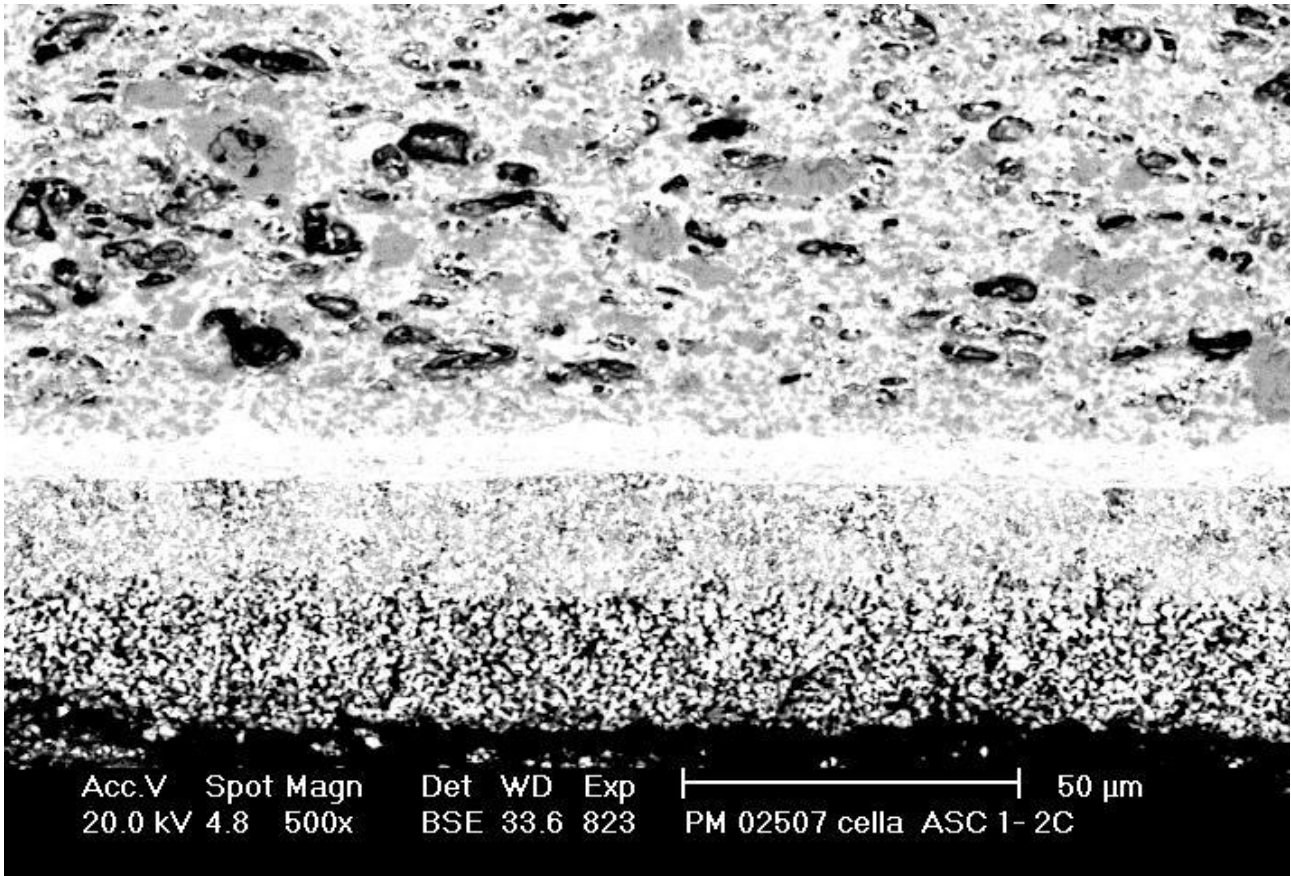
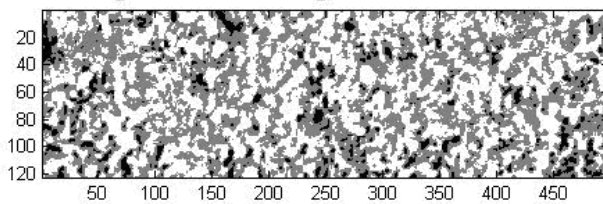
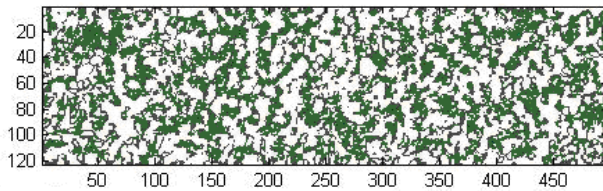


Figure 24 - SEM-BSE micrograph of the whole cell cross-section

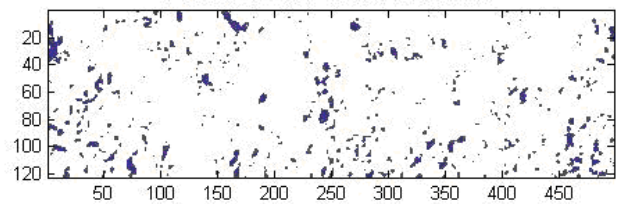
Thresholded original BSE/SEM Image - LSM/8YSZ active cathode layer



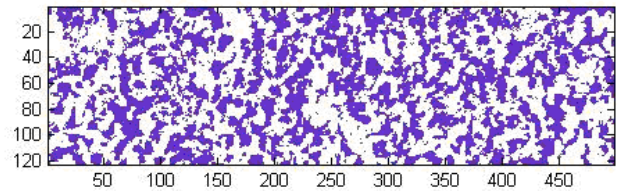
LSM Distribution - Volume Fraction: 48%



Pores Distribution - Volume Fraction 7%



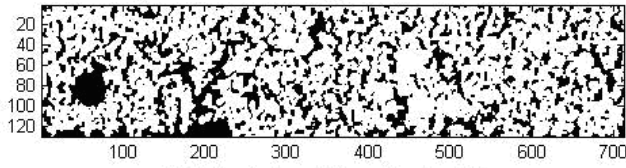
Zr Distribution - Volume Fraction: 45%



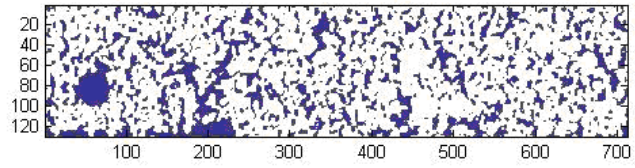
Pixels are the coordinates for both x-axes and y-axes in each figure

Figure 25. Solid and pore phase distribution and volume fraction estimated through image analysis of the cathode active layer

Thresholded original BSE/SEM Image - Porous LSM current collector



Pores Distribution - Volume Fraction 30%



LSM Distribution - Volume Fraction: 70%

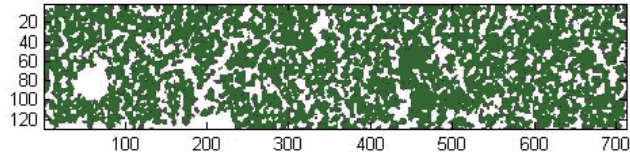


Figure 26. Solid and pore phase distribution and volume fractions estimated through image analysis of the cathode current collector layer

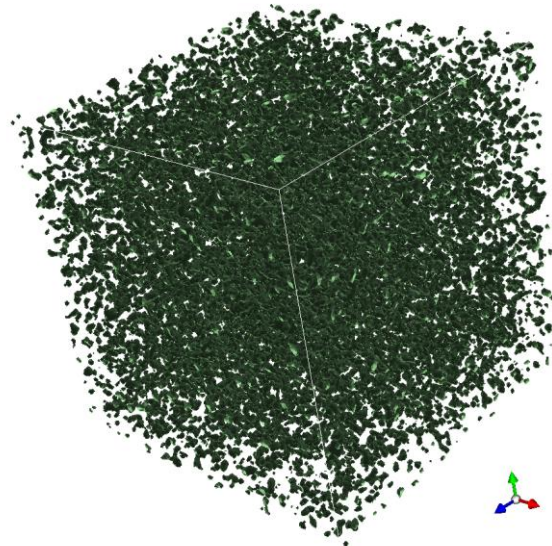
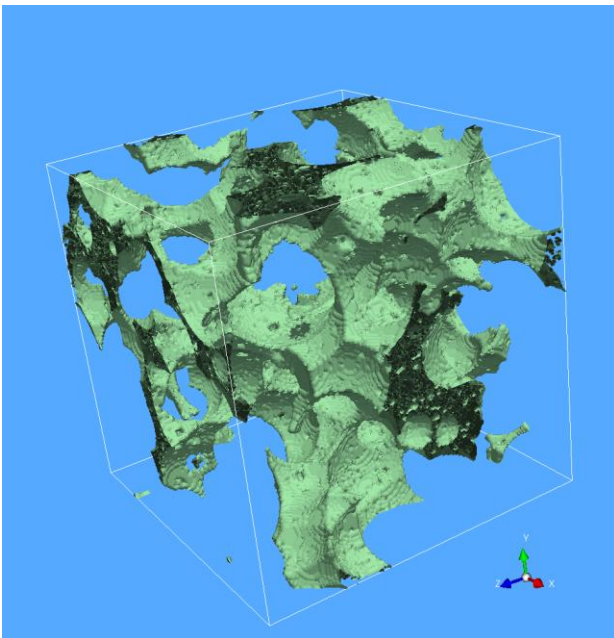


Figure 27- (left) 3D reconstruction of the porous cathode current collector layer (cube  $20 \times 20 \times 20 \mu\text{m}^3$ ); (right) close-up of the reconstructed structure

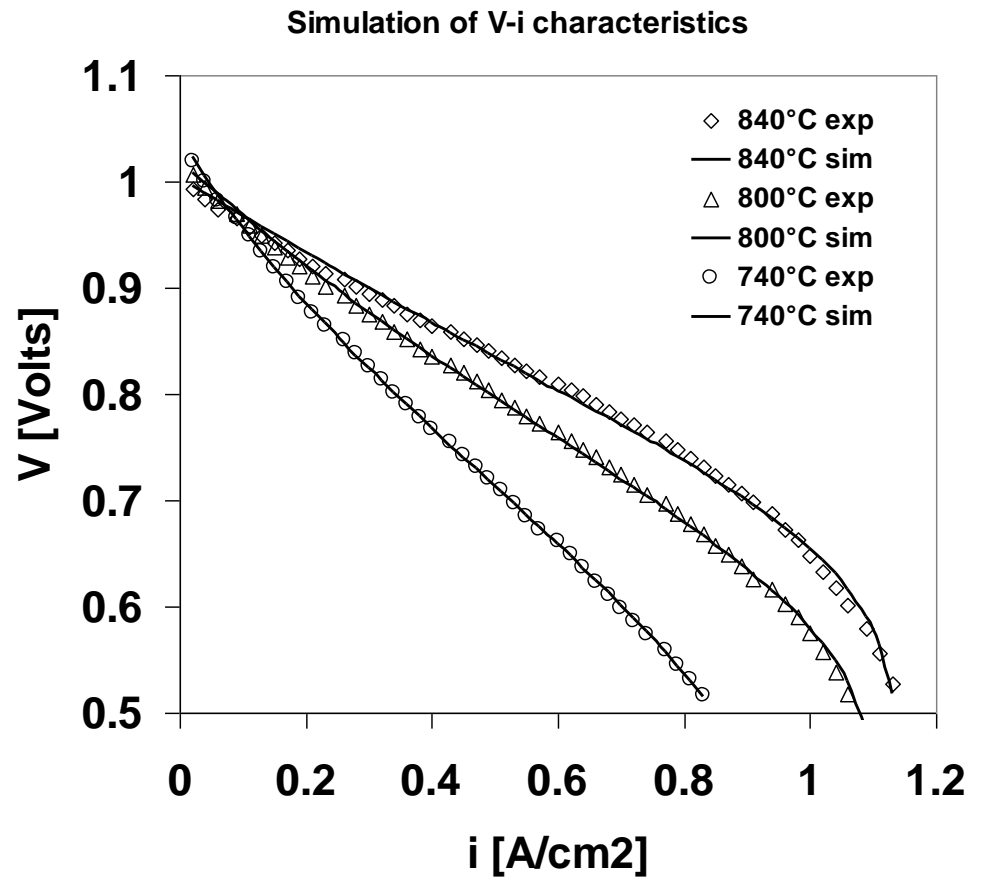


Figure 28. Experimental vs model behavior of anode-supported cell with LSM cathode



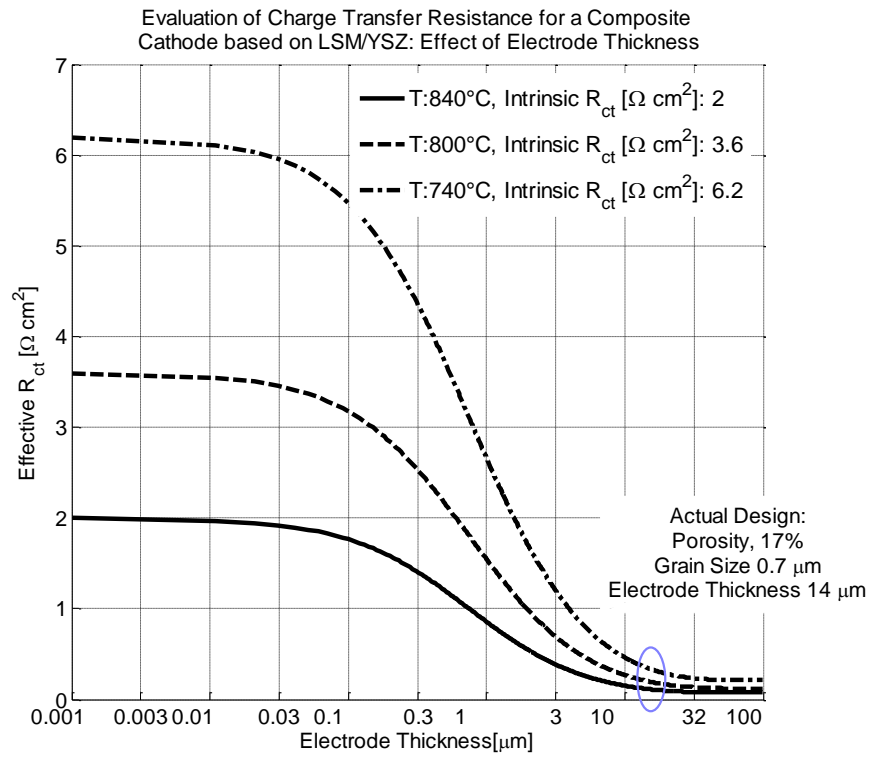


Figure 29. Evaluation of Effective Charge Transfer Resistance and its variation with electrode thickness

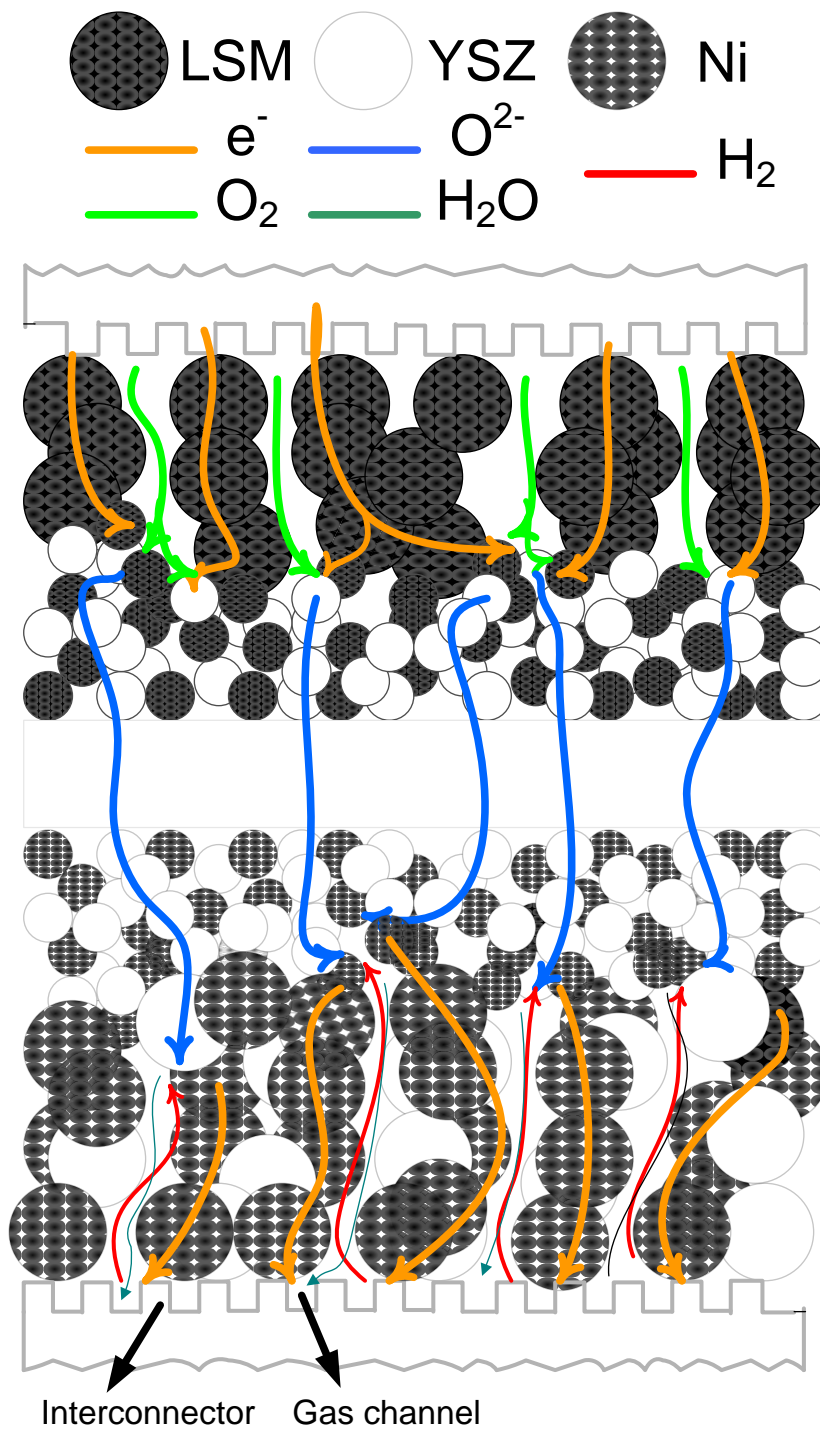


Figure 30. Schematic of an Solid oxide Fuel Cell considering composite electrodes as binary random packing of spheres (modelling particles)

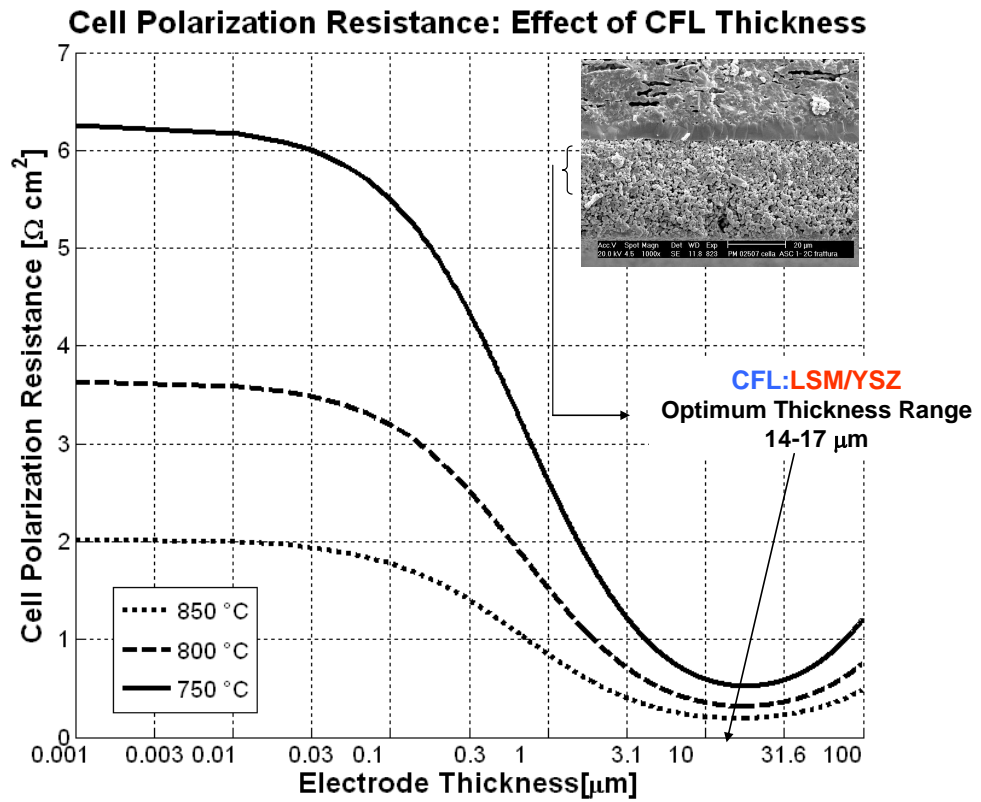


Figure 31. Cell polarization as a function of the CFL for different three operating temperatures